

CANUCS: Constraining the MACS J0416.1-2403 Strong Lensing Model with *JWST* NIRISS, NIRSpec and NIRCам

G. Rihtaršič¹, M. Bradač^{1,2}, G. Desprez³, A. Harshan¹, G. Noirot^{3,4}, V. Estrada-Carpenter³, N. S. Martis¹, R. G. Abraham^{5,6}, Y. Asada^{3,7}, G. Brammer^{8,9}, K. G. Iyer¹⁰, J. Matharu^{8,9}, L. Mowla¹¹, A. Muzzin¹², G. T. E. Sarrouh¹², M. Sawicki³, V. Strait^{8,9}, C. J. Willott¹³, R. Gledhill^{8,9}, V. Markov¹, and R. Tripodi¹

¹ Faculty of Mathematics and Physics, Jadranska ulica 19, SI-1000 Ljubljana, Slovenia
e-mail: gregor.rihtarsic@fmf.uni-lj.si

² Department of Physics and Astronomy, University of California Davis, 1 Shields Avenue, Davis, CA 95616, USA

³ Department of Astronomy & Physics and Institute for Computational Astrophysics, Saint Mary's University, 923 Robie Street, Halifax, NS B3H 3C3, Canada

⁴ Space Telescope Science Institute, 3700 San Martin Drive, Baltimore, Maryland 21218, USA

⁵ David A. Dunlap Department of Astronomy and Astrophysics, University of Toronto, 50 St. George Street, Toronto, Ontario, M5S 3H4, Canada

⁶ Dunlap Institute for Astronomy and Astrophysics, 50 St. George Street, Toronto, Ontario, M5S 3H4, Canada

⁷ Department of Astronomy, Kyoto University, Sakyo-ku, Kyoto 606-8502, Japan

⁸ Cosmic Dawn Center (DAWN), Denmark

⁹ Niels Bohr Institute, University of Copenhagen, Jagtvej 128, DK-2200 Copenhagen N, Denmark

¹⁰ Columbia Astrophysics Laboratory, Columbia University, 550 West 120th Street, New York, NY 10027, USA

¹¹ Whittin Observatory, Department of Physics and Astronomy, Wellesley College, 106 Central Street, Wellesley, MA 02481, USA

¹² Department of Physics and Astronomy, York University, 4700 Keele St. Toronto, Ontario, M3J 1P3, Canada

¹³ National Research Council of Canada, Herzberg Astronomy & Astrophysics Research Centre, 5071 West Saanich Road, Victoria, BC, V9E 2E7, Canada

Received ...; accepted ...

ABSTRACT

Context. Strong gravitational lensing in galaxy clusters has become an essential tool in astrophysics, allowing us to directly probe the dark matter distribution and study magnified background sources. The precision and reliability of strong lensing models rely heavily on the number and quality of multiple images of background sources with spectroscopic redshifts.

Aims. We present an updated strong lensing model of the galaxy cluster MACS J0416.1-2403 with the largest sample of multiple images with spectroscopic redshifts in a galaxy cluster field to date. Furthermore, we aim to demonstrate the effectiveness of *JWST*, particularly its NIRISS camera, for strong lensing studies.

Methods. We use the *JWST*'s NIRCам imaging and NIRSpec and NIRISS spectroscopy from the CANadian NIRISS Unbiased Cluster Survey (CANUCS). The cluster mass model is constrained using `Lenstool` software.

Results. Our new dataset, used for constraining the lens model, comprises 303 secure multiple images from 111 background sources and includes systems with previously known MUSE redshift and systems for which we obtained spectroscopic redshift for the first time using NIRISS and NIRSpec spectroscopy. The total number of secure spectroscopic systems is $> 20\%$ higher than in the previous strong lensing studies of this cluster. The derived strong lensing model can reproduce multiple images with the root-mean-square distance of $\sim 0''.53$. We also provide a full catalogue with 415 multiple images, including less reliable candidates. We furthermore demonstrate the effectiveness of *JWST*, particularly NIRISS, for strong lensing studies. As NIRISS F115W, F150W, and F200W grism spectroscopy captures at least two of the [OII] $\lambda 3727$, [OIII] $\lambda \lambda 4959, 5007$, and H_α lines at $1 \lesssim z \lesssim 3$ (a redshift range particularly relevant for strong lensing studies) without target pre-selection, it complements MUSE and NIRSpec observations extremely well.

Key words. gravitational lensing: strong – galaxies: distances and redshifts – galaxies: clusters: individual: MACS J0416.1-2403

1. Introduction

Strong gravitational lensing of cluster-size lenses has become an important tool in astrophysics. It provides large magnifications that allow us to study faint galaxies and sub-kpc regions at high redshifts that would otherwise be inaccessible with current telescopes. It thus offers an insight into the formation of first galaxies and the sources of reionisation (e.g. Hashimoto et al. 2018; Vanzella et al. 2023; Welch et al. 2023; Asada et al. 2023; Strait et al. 2023; Mowla et al. 2024; Adamo et al. 2024; Bradač et al. 2024; Fujimoto et al. 2024). In extreme cases it even en-

ables studies of individual stars over cosmological distances (e.g. Welch et al. 2022; Meena et al. 2023; Fudamoto et al. 2024; Furtak et al. 2024). Since gravitational lensing allows us to estimate mass distribution independently of the hydrostatic equilibrium and dynamical equilibrium of cluster galaxies, it is also an essential tool for investigating the interplay between baryons and dark matter on different scales and characterising properties of merging and out-of-equilibrium clusters (see Natarajan et al. 2024 for a review). Finally, since lensing depends on the geometry of the Universe, it can also be utilised to constrain values of cosmo-

logical parameters (e.g. Refsdal 1964; Jullo et al. 2010; Magaña et al. 2018; Caminha et al. 2022a).

The various applications of strong lensing rely on an accurate reconstruction of the mass distribution, which, in turn, relies on the quality and abundance of data: positions and accurate redshifts of multiple images of strongly lensed background sources. This first requires high-resolution imaging in several photometric bands, which enable precise position measurements and multiple image system identification based on colours and morphologies. It also requires spectroscopic redshift measurements, which are essential for confirming multiple images and reducing systematic errors (e.g. Johnson & Sharon 2016). Until recently, the progress in the field of strong lensing in galaxy clusters was spearheaded by the Hubble Space Telescope (*HST*) with its large field of view and high-resolution imaging in the visible wavelengths, complemented by ground-based spectroscopic observations (e.g., with VLT’s Multi-Unit Spectroscopic Explorer - MUSE, Bacon et al. 2012). The James Webb Space Telescope (*JWST*), launched in 2021, expanded those capabilities to near infra-red wavelengths, paving the way for a new generation of lens models (e.g. Caminha et al. 2022b; Mahler et al. 2023; Furtak et al. 2023; Diego et al. 2023a; Gledhill et al. 2024).

The CANadian NIRISS Unbiased Cluster Survey (CANUCS) is a ~ 200 h survey aiming to use the unprecedented capabilities of *JWST* in combination with strong gravitational lensing in galaxy clusters to study high redshift galaxies. With three of the four instruments onboard *JWST*, CANUCS observed 5 massive clusters known to be effective gravitational lenses, including MACS J0416.1-2403 (hereafter MACS0416).

MACS0416 is a massive galaxy cluster at $z = 0.397$, discovered by the MASSive Cluster Survey (MACS, Ebeling et al. 2010). MACS0416 is a cluster merger featuring a two-peaked X-ray surface brightness distribution (Mann & Ebeling 2012) coinciding with a bimodal mass distribution and is likely in a pre-collisional phase (Balestra et al. 2016). Due to its elongated mass distribution and large Einstein radius, MACS0416 is a very effective gravitational lens and has, since its discovery, been targeted by several cluster surveys. It was selected as a part of the Cluster Lensing and Supernova survey with Hubble (CLASH, Postman et al. 2012), which provided constraints for the first detailed mass model by Zitrin et al. (2013). Due to its essential lensing properties, MACS0416 was among the 6 clusters observed as a part of the Hubble Frontier Fields (HFF) program (Lotz et al. 2017, 2014), which provided deep ($\lesssim 28.5$ mag) imaging data in seven *HST* ACS/WFC3 bands of the central cluster region. The HFF imaging data has since been used in numerous lensing analyses (e.g. Jauzac et al. 2014, 2015; Johnson et al. 2014; Diego et al. 2015; Kawamata et al. 2016). The extended cluster region was also observed by The Beyond Ultra-deep Frontier Fields and Legacy Observations (BUFFALO) program (Steinhardt et al. 2020).

MACS0416 has also been targeted by several spectroscopic follow-up observations. The cluster was observed with VLT/VIMOS as a part of the CLASH-VLT spectroscopic campaign (presented in Balestra et al. 2016), resulting in a lens model constrained with 30 spectroscopically confirmed multiple images, belonging to 10 systems (Grillo et al. 2015, see Table 5). *HST*/WFC3 infrared grism spectroscopy, obtained by the Grism Lens-Amplified Survey from Space (GLASS, Treu et al. 2015; Schmidt et al. 2014), led to a non-parametric lens model and a dataset of 30 spectroscopic multiple images of 15 background sources (Hoag et al. 2016). A substantial improvement of multiple image catalogue was facilitated by several VLT/MUSE

Catalogue	N_{sys}	N_{im}	Spec. measurement
Grillo et al. (2015)	10	30	VLT/VIMOS
Hoag et al. (2016)	15	30	<i>HST</i> /GLASS
Caminha et al. (2017)	37	102	VLT/MUSE
Bergamini et al. (2021)	66	182	
Richard et al. (2021)	71	198	
Be23	88	237	
Di23 (PEARLS)	77	226	
This work - gold	111	303	<i>JWST</i> /CANUCS
This work - all	124	349	

Table 1: The number of systems N_{sys} and multiple images N_{im} with known spectroscopic redshift from several strong lensing studies. The last column represents the name of the survey or the instrument used to improve the catalogue of spectroscopic systems. Some studies use the same data but differ in the number of systems and images, either due to different quality assessments or due to the inclusion of multiply imaged clumps within a single background galaxy. The number does not include systems without spectroscopic redshifts, which were also used to constrain the lens model in some works (e.g. Di23). Note that the last line (this work - all) also includes images from the quartz catalogue with MUSE redshift, which are not used for lens modelling.

observations. The southwest region of the cluster was observed with MUSE as a part of the programme 094.A-0525 (PI: Bauer) with 11h of exposure time. The northeast region has been targeted by the programs GTO 094.A-0115B (PI: Richard) and 0100.A-0764 (PI: Vanzella, Vanzella et al. 2021), reaching the total integration time of 17.1h. This makes MACS 0416 a cluster with some of the deepest MUSE observations to date.

Caminha et al. (2017) presented a catalogue of 102 spectroscopically confirmed multiple images from 37 sources leveraging the first MUSE observations. Their model was improved by including hot X-ray emitting gas component (Bonamigo et al. 2017, 2018) and information on galaxy kinematics (Bergamini et al. 2019). The dataset of multiple images was further expanded by Bergamini et al. (2021), leveraging the data presented in Vanzella et al. (2021). Richard et al. (2021) published a MUSE catalogue of 198 multiple images from 71 systems. This number was further increased to 237 spectroscopically confirmed multiple images by Bergamini et al. (2023) (henceforth Be23). Another catalogue of 214 multiple images was compiled by Diego et al. (2023b) by reevaluating systems from existing literature. Before the onset of *JWST*, these catalogues presented the most extensive dataset of spectroscopically confirmed multiple images for this cluster. They are a starting point for constructing the initial catalogue used in our search for additional multiple-image systems.

MACS0416 was recently observed with *JWST*/NIRCam by the CANUCS survey and the Prime Extragalactic Areas for Reionization and Lensing Science (PEARLS, Windhorst et al. 2023), covering the wavelength range from 0.8 to 5 μm . Three epochs of observations of the PEARLS program with an additional CANUCS epoch have enabled studies of transient events in highly magnified regions of lensed galaxies (e.g., Yan et al. 2023; Diego et al. 2023c). During the preparation of this paper, the PEARLS collaboration published a new lens model constrained leveraging the new *JWST* imaging data (Diego et al. 2023a) (henceforth Di23). With 343 multiple image candidates, belonging to 119 multiple image systems, the Di23 catalogue

represents the largest such dataset to date. It contains all previously known systems with MUSE spectroscopic redshift, as well as 41 additional candidates without spectroscopic confirmation. We used their catalogues to supplement our dataset, which we further expanded with our imaging and spectroscopic data. For easier comparison of our works, we cross-matched our catalogues and adopted their names of multiple image systems.

In addition to NIRC*am* imaging, the CANUCS program also includes Near Infrared Imager and Slitless Spectrograph (NIRISS, Doyon et al. 2012) wide field slitless spectroscopy in the F115W, F150W and F200W bands, as well as Near Infrared Spectrograph (NIRSpec) multi-object prism spectroscopy. The new spectroscopic data obtained with *JWST* are the basis of this work.

In Table 1, we list catalogues from several strong lensing studies with the number of multiple images and multiple-image systems.

Throughout this work we assume a flat Λ CMD cosmology with $\Omega_\Lambda = 0.7$, $\Omega_m = 0.3$, and $H_0 = 70 \text{ km s}^{-1} \text{ Mpc}^{-1}$. At the cluster redshift $z = 0.396$, a projected distance of $1''$ corresponds to a physical scale of 5.340 kpc. Magnitudes are given in the AB system (Oke & Gunn 1983).

2. Data

2.1. Imaging & photometry

In this work we use CANUCS NIRC*am* observations in filters F090W, F115W, F150W, F200W, F277W, F356W, F410M, and F444W with 6.4 ks exposure time per filter. In addition, we use the archival *HST*/ACS imaging data in F435W, F606W, and F814W filters and *HST*/WFC3 data in F105W, F110W, F125W, F140W, F160W filters from the HFF (Lotz et al. 2017, 2014) and CLASH (Postman et al. 2012) programs. The data reduction and production of the photometric catalogues follows the procedure outlined in Noirot et al. (2023) and Asada et al. (2024). The NIRC*am* and WFC3 images were first processed with the official STScI *JWST* pipeline and Grizli (Brammer 2023) and drizzled on the same pixel scale (40 mas/pixel) and aligned with Gaia DR3 astrometry (Gaia Collaboration et al. 2016, 2023). The diffuse cluster light and the bright cluster galaxies were modelled and removed following the procedure described in Martis et al. (2024). The bright cluster galaxy subtracted images were then PSF-homogenised to match the PSF in the F444W filter. Source detection was performed on the χ_{mean} detection image (Drlica-Wagner et al. 2018). Photometric catalogues were produced with the Photutils package (Bradley et al. 2023) using Kron (Kron 1980) and fixed apertures of different sizes. Photometric redshifts were computed with EAZY-py (Brammer et al. 2008) using the latest standard templates (tweak_fsps_QSF_12_v3) and templates from Larson et al. (2023). EAZY-py also returns the "risk" value $z_{\text{phot_risk}}$, as defined in Tanaka et al. (2018), which we use as an indicator of the photometric redshift reliability. In this work, we only show photometric redshifts with $z_{\text{phot_risk}} > 0.2$ (Sect. 3.1).

2.2. NIRISS grism spectroscopy

The cluster was observed with NIRISS using Wide-Field Slitless Spectroscopy (WFSS) mode (Willott et al. 2022) in F115W, F150W and F200W filters and two orthogonal grisms (GR150C and GR150R, $R \sim 150$) with 9.7 ks exposure time per configuration. Data reduction follows the procedure described in Noirot et al. (2023) and includes the initial processing and source

modelling with Grizli. The contamination of the cluster galaxies is modelled using the isophotal models of the bright cluster galaxies (Sect. 2.1) and subtracted from the spectra (the procedure is described in Estrada-Carpenter et al. 2024). We use our Photutils catalogues from NIRC*am* images to obtain the positions of sources and their spectra. The continuum of each source is then modelled using an iterative polynomial fit. The contamination from other sources is subtracted from the spectrum of each source in the catalogue. The redshift is fitted using the procedure described in Noirot et al. (2023). Each source is fitted with three different methods. The first method fits the spectra using a narrow spectral range ($1.03 - 1.26 \mu\text{m}$ in F115W, $1.35 - 1.65 \mu\text{m}$ in F150W, $1.79 - 2.20 \mu\text{m}$ in F200W) to avoid the less sensitive regions at the edges of each filter response curve. The second method uses the full spectral range to reliably fit sources with emission lines with wavelengths close to the edges of the filter response curves. The third method is a joint fit of the spectro-photometric data with Grizli using all available *JWST* NIRISS, NIRC*am* and *HST* filters. The obtained grism redshifts z_{niriss} are prioritised in that order and are selected upon visual inspection of each spectral fit and assessment of its quality. For some sources, none of the three fits returned a reliable redshift. Those sources were refitted with custom modification of the data range (e.g., by removing configuration with visible unsubtracted contamination) or by applying narrower redshift priors and then visually reinspected. The grism spectra used in this work are provided in Appendix A together with details of the individual fits.

While Grizli provides a redshift probability density function, its width likely underestimates the true redshift uncertainty (see Noirot et al. 2023). To account for the possible systematic errors we compare grism redshifts of known multiple images with their MUSE redshifts z_{muse} from Richard et al. (2021) catalogue. We find that all grism redshifts apart from the two outliers K8 and K5 (see Sect. 3.2) match MUSE redshift within $\delta z_{\text{niriss}} = \pm 0.005(1 + z_{\text{spec}})$ which we use as an error estimate. This error encompasses a small systematic offset - we found that our NIRISS redshifts z_{niriss} may be, on average, underestimated by $\sim 0.002(1 + z_{\text{spec}})$ when compared with z_{muse} . While this issue will be further investigated before the release of the CANUCS NIRISS redshift catalogues, we note that this difference is of negligible consequence for the strong lensing analysis.

In Sect. 3.2 (see Fig. 2), we also utilise spatially resolved emission line maps to match (if applicable) different subcomponents of each multiple image. Maps are obtained as described in Estrada-Carpenter et al. (2024). To this end, the extended source is first segmented based on pixel SNR. All regions are then fitted simultaneously with priors obtained with broadband photometry and by using a linear combination of spectral templates. The emission line maps are obtained by forward modelling the galaxy with the best-fit model, excluding the line of interest, subtracting it, and dithering the residuals.

2.3. NIRSpec prism spectroscopy

Following the NIRC*am* and NIRISS observations, their reduction and subsequent target selection, MACS0416 was observed with NIRSpec using the PRISM/CLEAR disperser with nominal resolving power ~ 100 and the approximate wavelength coverage between 0.6 and $5.3 \mu\text{m}$. Targets were selected for a variety of science goals, including multiple-image system candidates for this project (see Sect. 3.1), and were observed through the Micro-Shutter Assembly (MSA) with 2.9 ks exposures for each MSA configuration. The cluster was observed with three MSA configurations. The data is then processed using the STScI

JWST pipeline and the *msaexp* package (Brammer 2022). This includes mitigating the snowball residuals, masking out pixels approaching saturation, standard wavelength calibration, flat-field and path-loss corrections, photometric calibration and the extraction of 1-D spectra (e.g. see Withers et al. 2023, and Desprez et al. 2024 for a more detailed outline of the procedure). The redshifts z_{nirspec} were also obtained using *msaexp*. In Appendix B, we show the NIRSpec spectra used in this work and describe cases that required distinct treatment.

The NIRSpec redshift uncertainty was estimated by comparing the NIRSpec with MUSE redshift from Richard et al. (2021), similarly to Sect. 2.2. We found that the difference between MUSE and NIRSpec redshift is below $0.002(1 + z_{\text{spec}})$ for more than 68% of multiple images. We use this as an error estimate, which takes into account potential small systematic deviations (e.g. Bunker et al. 2023). As a test, we also estimated the uncertainty by fitting a Gaussian profile to the strongest spectral line in spectra of several objects and obtained the line position uncertainty. We find it to be consistent with our error estimate.

3. CATALOGUE OF MULTIPLE IMAGES

In this section, we describe our catalogue of strong lensing constraints and the methods used to obtain them. Based on reliability, we divide our catalogue in several categories. The gold category, which is used for lens model optimisation, is the most secure and encompasses reliable images from existing catalogues with MUSE redshift z_{muse} (see Sect. 3.2) and new spectroscopic systems, which we trust either due to multiple spectroscopic redshift measurements with NIRISS or NIRSpec, morphology, photometric redshift or/and lensing configuration. It contains 303 images from 111 multiple image systems. We also provide a catalogue of less reliable sources which may be of interest for future studies. These sources are divided into silver or bronze categories with intermediate and low degrees of confidence, respectively. We also add a fourth category of quartz images. Those images appear in previous works with measured MUSE redshift but are excluded from our gold category because we cannot reliably identify or confirm them with our NIRCам imaging (see Sect. 3.2). The total number of multiple images in all catalogues is 415, belonging to 150 systems (124 with spectroscopic redshifts). This makes our catalogue the largest catalogue of multiple images in a galaxy cluster field to date. The number of secure spectroscopic multiple images in our gold category transcends the number obtained with MUSE data (Be23) by 28%. The catalogues of spectroscopic lensing constraints from previous studies are summarised in Table 1. In Fig. 1, we show the *HST* & *JWST* image of the central region of MACS0416, overlaid with our lensing catalogue.

Multiple images in our catalogue are labelled as follows. New CANUCS systems are denoted with the prefix C. Previously known systems are denoted with the prefix K and the identifier from Di23, allowing for a straightforward cross-matching of the catalogues. The lowercase letter following the main ID is the label of the multiply-imaged clump. We note that each clump is considered a separate system when reporting the total system count. The decimal digit represents the image ID. For instance, image K14b.3 is the third image of the second (b) clump of a galaxy with ID 14 in Di23 catalogue.

We assign systems with at least one spectroscopic redshift measurement, a system redshift z_{sys} , which is used for lens modelling. If MUSE redshift is available, we set $z_{\text{sys}} = z_{\text{muse}}$ due to its higher spectral resolution compared to NIRSpec and NIRISS (except in systems K5 and K8 where we update the spectro-

scopic redshift; see Sect. 3.2). If z_{muse} is unavailable, we use z_{niriss} , z_{nirspec} or the mean of the two if both are available, due to their comparable spectral resolutions. We note that the redshift differences between different measurements are small and have a negligible impact on the lensing analysis.

Gold catalogue in *Lenstool* format, as well as the full catalogue with indicated gold, silver and bronze categories are available on CANUCS website¹ and will be available on Mikulski Archive for Space Telescopes (MAST)² with DOI 10.17909/ph4n-6n76 together with other CANUCS data products and lens models. Any relevant changes to the previous lensing catalogues are listed and described in the following subsections.

3.1. New multiple images

The search for new multiple images and multiple image systems was performed by leveraging the strong lensing model from Be23 which was constrained with over a hundred spectroscopically confirmed multiple images, uniformly distributed across the cluster field and covering a wide redshift range $1 \lesssim z \lesssim 6$. The model describes their catalogue of multiple images with root-mean-square distance $\Delta_{\text{rms}} = 0''.43$. We used the Be23 best model parameters to predict the positions of potential counter images of all sources in our photometric catalogues brighter than the 28.5 magnitude in F200W filter, using *Lenstool* and Eazy redshifts. The magnitude limit was applied to reduce computational and manual inspection time. It is motivated by the fact that identifying multiple image candidates based on colour and morphology similarity becomes increasingly difficult at fainter magnitudes. Each source with predicted multiple images was then visually inspected. We examined a region around the predicted counter images in several RGB combinations of the *HST* and *JWST* filters, trying to identify sources with similar colours, morphology or photometric redshift. The visually inspected region around each source was broad, spanning over $\sim 15''$ - much broader than Δ_{rms} of the model. This strategy was adopted to prevent any potential lensing model inaccuracies from biasing our dataset, as well as to account for errors in photometric redshifts. The regions around the source and image predictions were also checked for any neighbouring sources with similar configurations of multiple images, not predicted by the lens model either due to catastrophic redshift errors (e.g. with redshift below cluster redshift) or due to them not being included in our photometric catalogues. We note that a vast majority of multiple image systems in this cluster follow a similar configuration, forming a sequence of three multiple images oriented perpendicularly to the elongated cluster morphology.

After compiling a list of candidates for multiple image systems, we inspected their grism spectra and their fitted redshifts (see Sect. 2.2). The strategy for obtaining grism redshifts differed from the strategy used to obtain CANUCS grism redshift catalogues (Noirot et al., in prep.), where each of the spectra is evaluated independently. We jointly evaluated the spectra of each multiple-image system and used all of them to assess the reliability of individual redshifts or spectral features. For some images, we could identify a potential emission line in a single orientation only (for instance, if the other orientation was too contaminated). If the redshift obtained from such emission lines matched the spectroscopic redshift of other images within redshift uncertainty, we considered the candidate spectroscopically

¹ <https://niriss.github.io/>

² <https://archive.stsci.edu/>

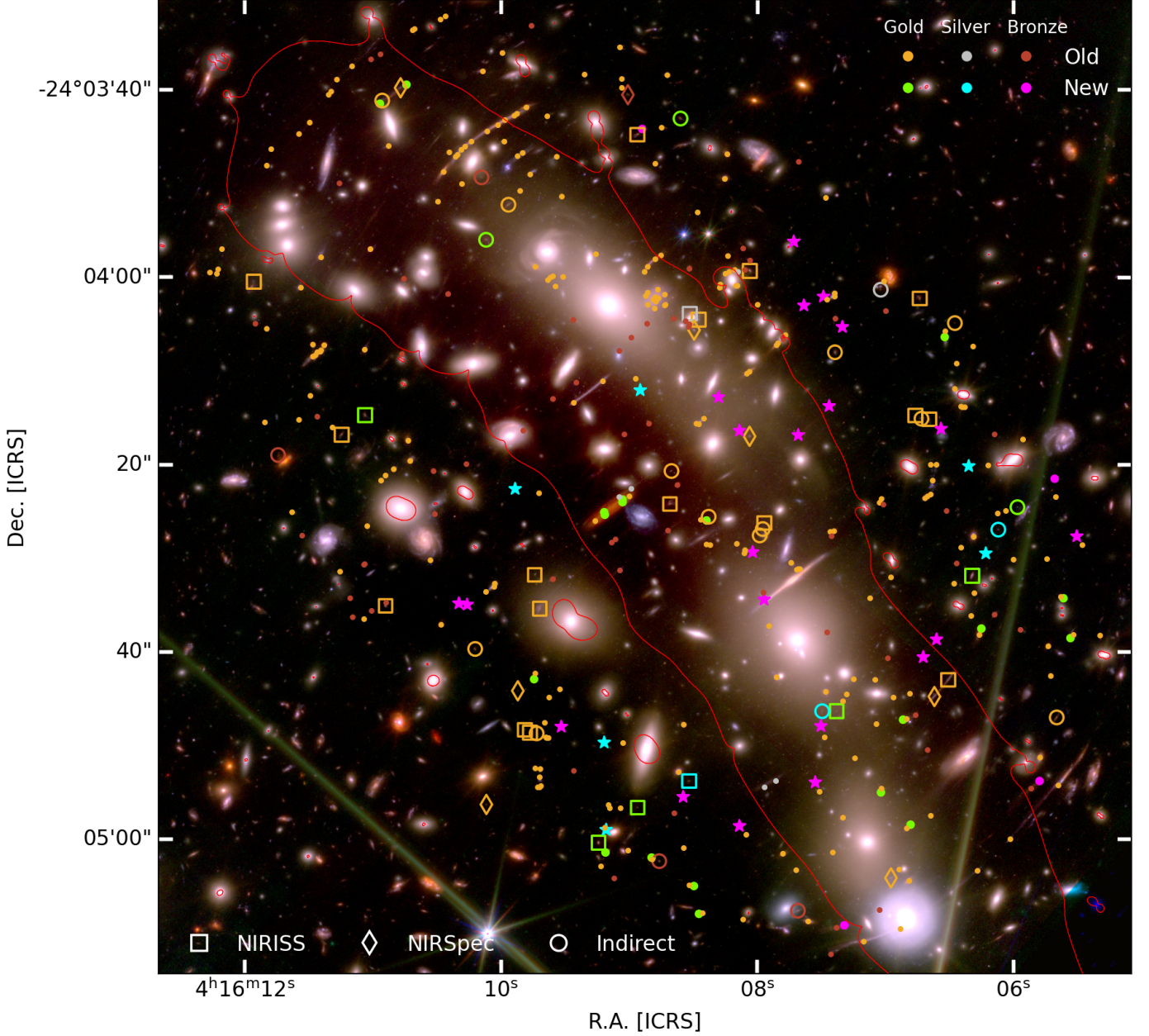


Fig. 1: *JWST*/NIRCam and *HST*/WCS image (F277W, F356W, F410M, F444W in red, F115W, F150W, F200W in green and F814W, F606W, F435W, F090W in blue) of the central region of MACS0416 with multiple images. Newly identified systems or multiply imaged clumps belonging to the gold, silver or bronze category are shown in green, cyan or magenta colour, respectively. Known systems and clumps from Di23 and Be23 are depicted in gold, silver or bronze with a colour corresponding to their catalogue in this work. The bronze category also includes quartz images. Squares and diamonds represent images with new spectroscopic redshift, obtained with NIRISS and NIRSpec, respectively. Empty circles represent images for which we could not measure spectroscopic redshift directly but have new spectroscopic redshifts inferred from other images of the system. Stars represent newly identified candidate systems for which we could not obtain spectroscopic redshift. The red solid line represents the tangential (outermost) critical curve from our lensing model for redshift $z = 9$.

confirmed. This approach allowed us to extract useful information from several spectra that would, on their own, prove inconclusive (see Appendix A). The newly found CANUCS systems with NIRISS spectroscopic redshifts are listed in Table 2.

After the initial search for multiple images we compiled the list of targets for spectroscopic follow-up observations with NIRSpec. The candidates were assigned priority values based on their reliability and unavailable grism redshifts. We note that our

degree of confidence in some systems was high enough (e.g. due to colour and morphology similarity) that they did not necessarily require spectroscopic confirmation of all images. In such cases, a single spectroscopic redshift was enough to include the system in the gold category of multiple images with z_{spec} . Due to the limited possible configurations of the three MSA masks and the large number of follow-up candidates, not all of our lensing candidates were observed. On the other hand,

Table 2: New CANUCS systems of multiple images with spectroscopic redshifts, found in this work with their ICRS coordinates, NIRISS redshifts and their class (gold or silver, depending on their reliability). Grism redshift uncertainty is estimated as $0.005(1+z)$ (see Sect. 2.2).

id	ra	dec	z_{niriss}	class
C1.1	64.026343	-24.075524	2.91	g
C1.2	64.038488	-24.083446	2.91	
C2.1	64.037222	-24.082402	3.07	g
C2.2	64.024868	-24.073494		
C2.3	64.030749	-24.079544	3.07	
C3.1	64.035827	-24.061968		g
C3.2	64.042150	-24.065565		
C3.3	64.046081	-24.070770	2.56	
C4.1	64.035547	-24.081619	1.86	s
C4.2	64.031217	-24.079546		
C4.3	64.025491	-24.074159		

we obtained NIRSPEC spectra of some images which were initially not identified as multiple image candidates (e.g., K100.1 at $z_{\text{nirspec}} = 7.24 \pm 0.02$).

After the release of the multiple image catalogue of the PEARLS collaboration (Di23), which leveraged *JWST* imaging data, we used it to assess the effectiveness of our multiple image identification method. As mentioned above, we cross-matched the catalogues and renamed our candidates to match the Di23 catalogues for a straightforward comparison. We independently found 20 multiple image system candidates from Di23. For 11 of them, we also obtained spectroscopic redshifts, which are listed in Table 3 with their class. Then, we visually inspected the remaining 22 system candidates from Di23, which we previously missed, and evaluated them, following the same procedure as before. We included systems K100, K99 and image K115a.3 in the gold catalogue. For systems K100 and K99 we also obtained spectroscopic redshift (see Table 3). We also added 1 new silver system and 4 new bronze systems. For consistency, we did not include other system candidates from Di23 in our catalogue as they were too faint or otherwise could not be confirmed with the same degree of confidence that we used for our candidates. Regardless, those candidates may still be interesting for future studies, so we direct the reader to Di23 for a full list.

In addition, we also found 15 systems not reported in Di23. For systems C1, C2, C3 and C4, we obtained grism redshifts and included C1, C2 and C3 in the gold category and C4 in the silver category. We provide a list of new multiple-image systems with spectroscopic redshifts in Table 2. For candidates from C5 to C15, we did not obtain spectroscopic redshifts. In Table 4, we provide their photometric redshifts and class. The class of the new multiple images was assigned upon qualitative assessment of the similarity of their colours in several *HST* and *JWST* RGB combinations (in Appendix A, we show cutouts of the new images), morphological features, their lensing configuration and photometric and spectroscopic redshifts.

In total, we identified 8 gold, 9 silver and 21 bronze new multiple images. We also applied our method of finding multiple images to the other cluster of the CANUCS survey (e.g. Gledhill et al. 2024, Desprez et al. in prep).

3.2. Known systems with MUSE redshift

Our initial catalogue of secure multiple images was compiled from Be23, Diego et al. (2023b), and Richard et al. (2021) catalogues, which were all based on *HST* imaging and VLT/MUSE observations, described in Sect. 1. A small correction ($\sim 0''.2$) was applied to positions from the previous catalogues to match the positions in our *JWST* images. We adopted the system names from Di23. We also include additional multiply lensed clumps from Be23, which provide additional information on image deformation and are particularly useful for constraining critical curves (e.g. Bergamini et al. 2021; Grillo et al. 2016). We keep the same order of clumps as in Be23 while indexing them with letters instead of numerals. For example, system 12.6 from Be23 corresponds to the clump K1f where the name K1 indicates the galaxy with ID 1 in Di23. All systems were visually inspected in the *JWST* data and assigned to the gold or quartz category. The quartz systems, which were considered reliable in Di23, but are excluded from the gold category in this work, include systems K27, K28, K51, K56, K58, K59, K60, K61, K75 and the images K25.2, K45.3, K57.3. Some of those sources were excluded from the gold category because they are not detected or are extremely faint (e.g. K51, K61, K75) or obscured by a foreground galaxy (K27.1). We also downgraded clump c of system K62 (corresponding to images 21.3b and 21.3c in Be23) to the quartz category due to faintness. We note that the candidates in the quartz system were not rejected by our study; we excluded them from the gold category since our data alone did not provide a sufficient degree of confidence. In some cases Be23 and Di23 select different candidates for the same image or report significantly different positions ($\geq 0''.3$). In such cases, we pick a more reliable candidate based on similar morphology or clear detection and add it to the quartz catalogue (K45.3, K58.1, K60.1, K61.3). We exclude the alternative candidates from all our catalogues - refer to Be23 and Di23 for a full list of candidates. Both images of system K59 at redshift $z = 4.530$ have different positions in Be23 and Di23 catalogues, with K59.2 candidates separated by more than $3''$. Despite clear detection of the Di23 candidate and absence of Be23 candidate in the NIRCcam data, we opted to include the latter in the quartz catalogue as it more closely matches the MUSE detection (see Richard et al. 2021). We also exclude K59.3 candidate from all catalogues as it was detected as a possible counterimage of Di23 candidates.

In a few spectroscopically confirmed extended systems we were not able to unambiguously identify multiply imaged features with our imaging data. An example is system K1 at redshift $z = 0.94$ (Hoag et al. 2016; Caminha et al. 2017), which contains a large extended arc. The arc is close to the northern brightest cluster galaxy (BCG) which increases the probability of microlensing events. Hence, it has been studied extensively due to its abundance of caustic-crossing transients (Chen et al. 2019; Kaurov et al. 2019; Chen et al. 2019; Kelly et al. 2022; Yan et al. 2023). The counterimage of the arc (K1a.3) is spectroscopically confirmed (Caminha et al. 2017) and is lensed by the cluster member with ID 8971 (ID from Be23, see Sect. 4). However, as it is difficult to securely identify exact counterparts of individual clumps in the arc with *HST* and *JWST* images, we decided to include the counterimage in the bronze category using the position from Di23 (the image was excluded on the same grounds from Bergamini et al. 2021 and Be23 lens models).

We find a similar situation in system K8 which comprises a very red arc and a spiral galaxy at redshift $z = 2.04$. The arc has also been investigated by Di23 as it hosted two extremely magnified star candidates. The system has a strong H_α emis-

Table 3: Multiple image candidates from Di23 with new CANUCS spectroscopic redshifts. System redshift z_{sys} , used for lens modelling is the average of NIRISS redshift z_{niriss} and NIRSspec redshift z_{nirspec} . All images of the system are in the same class (gold, silver or bronze, depending on their reliability) as the first image, unless explicitly indicated otherwise. The redshift uncertainty is estimated as $0.005(1+z)$ and $0.002(1+z)$ for z_{niriss} and z_{nirspec} , respectively (see Sects. 2.2 and 2.3).

id	ra	dec	z_{niriss}	z_{nirspec}	z_{sys}	class
K82.1	64.027117	-24.078617	2.03		2.04	g
K82.2	64.027568	-24.079111		2.043		
K82.3	64.036516	-24.083995				b
K87.1	64.028044	-24.067304	2.91		2.91	g
K87.2	64.036172	-24.073404	2.91			
K87.3	64.040400	-24.076506	2.91			
K89.1	64.027990	-24.070869			3.08	g
K89.2	64.033151	-24.074143				
K89.3	64.040716	-24.080179	3.07	3.082		
K90.1	64.028186	-24.070777	3.06		3.07	g
K90.2	64.033103	-24.073967	3.07			
K90.3	64.040882	-24.080101	3.07			
K91.1	64.027739	-24.070888	3.07		3.07	g
K91.2	64.033250	-24.074333				
K91.3	64.040505	-24.080204				
K95.1	64.037234	-24.062446	2.33		2.33	g
K95.2	64.041423	-24.064525				
K95.3	64.046847	-24.071344	2.33	2.330		
K98.1	64.033581	-24.071393		2.303	2.30	g
K98.2	64.030804	-24.068900				
K98.3	64.042504	-24.077700				
K99.1	64.040567	-24.075502	2.51		2.51	g
K99.2	64.036119	-24.072422				
K99.3	64.029316	-24.067045				s
K100.1	64.041116	-24.078943		7.24	7.24	g
K100.2	64.034910	-24.073778				
K100.3	64.026904	-24.068034				
K106.1	64.033572	-24.066483	2.70		2.71	g
K106.2	64.035385	-24.068243		2.712		
K106.3	64.045416	-24.076423	2.70			
K109.1	64.032006	-24.085463			2.16	b
K109.2	64.028979	-24.084492		2.160		g
K109.3	64.023589	-24.079729				g
K115a.1	64.044930	-24.061056		2.298	2.30	g
K115a.2	64.045528	-24.061436				
K115a.3	64.049699	-24.066808	2.30			
K115b.1	64.044751	-24.060955				
K115b.2	64.045622	-24.061524				
K97.1	64.037538	-24.061262		5.99	5.99	b
K97.2	64.042299	-24.063712				
K97.3	64.048913	-24.071950				

sion line in the F200W NIRISS grism channel, enabling a reliable spectroscopic redshift measurement with NIRISS in both the arc and counterimage. A part of the arc has also been observed with NIRSspec, confirming the spectroscopic redshift of $z_{\text{nirspec}} = 2.046 \pm 0.001$ (see Table 5 and Fig. B.2 and A.3 in the Appendix). The updated redshift differs from the previ-

ously measured MUSE redshift ($z_{\text{muse}} = 1.953$, see Table B.4 in Richard et al. 2021) by 0.09, which is above our redshift uncertainty. Furthermore, we identified the counterpart of the brightest clump of the arc in the counterimage. To this end, we examined several RGB combinations of *JWST* and *HST* filters, two of which are shown in Fig. 2. Additionally, we produced the map of

Table 4: New CANUCS system candidates without spectroscopic redshifts with their ICRS coordinates, Eazy photometric redshifts and category (silver or bronze, depending on their reliability). We only show the images from our photometric catalogues with $z_{\text{phot_risk}} > 0.2$ and with redshifts higher than the cluster redshift.

id	ra	dec	z_{phot}	
C5.1	64.037140	-24.070012		(s)
C5.2	64.041213	-24.072947	1.64	
C5.3	64.032164	-24.065615		(b)
C6.1	64.025908	-24.074851	2.83	(s)
C6.2	64.038250	-24.083050		
C7.1	64.026463	-24.072264	2.38	(s)
C7.2	64.038313	-24.080469	2.10	
C7.3	64.033115	-24.076220		(b)
C8.1	64.042781	-24.076381	1.93	(b)
C8.2	64.031192	-24.067244		
C9.1	64.033488	-24.074815	2.78	(b)
C9.2	64.039707	-24.080002	2.63	
C9.3	64.027375	-24.071157		
C10.1	64.031831	-24.067497	2.19	(b)
C10.2	64.034607	-24.070214		
C10.3	64.043043	-24.076331	1.90	
C11.1	64.027502	-24.077402	3.38	(b)
C11.2	64.027948	-24.077922		
C12.1	64.035741	-24.082074	2.17	(b)
C12.2	64.031260	-24.079980		
C13.1	64.030579	-24.068140	3.38	(b)
C13.2	64.033930	-24.071216		
C14.1	64.033924	-24.082935		(b)
C14.2	64.031458	-24.081651	3.42	
C14.3	64.022955	-24.074347	3.31	
C15.1	64.030995	-24.070493	3.04	(b)
C15.2	64.032010	-24.071340		

H_{α} emission line flux from F200W grism spectrum (spectrum is shown in Fig. A.3 and the emission line map in the right panel of Fig. 2). The brightest clumps a.2 and a.3 in the arc show clear H_{α} emission. The emission is expected to be higher than its counterpart a.1 in the spiral image due to higher magnifications in the arc. This rules out two of the brightest H_{α} emitting clumps above and below the galactic centre. Based on colour similarity and faint H_{α} emission, we identify the clump on the bottom left relative to the galactic centre to be the most likely candidate for clump a.1. We verified that given the shape of the caustic and the positions of bright clumps in the source plane, the selected a.1 clump is the furthest below the caustic line, i.e., is one of the most likely to be multiply imaged. Unlike K8a.1, we could not securely identify fainter counter images K8b.1 and K8c.1 to clumps K8b and K8c in the arc.

We did a minor correction to the spectroscopic redshift of system K5. Each of the three images of system K5 shows clear [OIII] $\lambda\lambda 4959, 5007$ (blended at the grism resolution), [OII] $\lambda 3727$ and H_{α} emission lines in the grism spectrum (see Fig. A.3, yielding spectroscopic redshift of $z_{\text{niriss}} = 1.84 \pm 0.01$, which dif-

fers from $z_{\text{muse}} = 1.8178$ (Richard et al. 2021) by more than our redshift uncertainty estimate.

We also spectroscopically confirmed image K62b.3, which was reported in Di23 (62.c) as a candidate. We measured $z_{\text{nirspec}} = 5.14 \pm 0.01$ and included it in the gold category with system redshift set to $z_{\text{muse}} = 5.106$. In system K26 we identified an alternative candidate to K26.3 from Di23. The grism spectrum (see Fig. A.3) of our candidate shows the [OIII] emission, yielding $z_{\text{niriss}} = 2.92 \pm 0.02$. This agrees with $z_{\text{muse}} = 2.9259$ hence we included our candidate in the gold catalogue. All relevant updates to known systems with MUSE redshifts are summarised in Table 5. We also modified some of the known systems without spectroscopic redshift from Di23. We provide our alternative candidate K81.3 to image 81.c from Di23 as well as a new counter image K96.3 of system K96. Both image candidates were found using the method described in Sect. 3.1 and are listed in Table 5.

In some multiple images with resolved structure in our imaging data, we included different features as separate multiple image systems. This includes several features in highly magnified arcs, included in Be23 as well as additional new families K8b, K8c, K22b, K49b, K55b, K64b, K85b and K115b. Out of those, K8b, K8c and K115b are situated in strongly lensed arcs and are useful for locally constraining the critical curves. Others belong to well-separated images and provide additional information on their orientation and local deformations.

K33 and K77 (14.1 and 14.2 in Be23) are a unique lensing system consisting of two compact low luminosity star-forming stellar complexes at redshift 3.221 (Vanzella et al. 2017). The sources are first multiply lensed by the global cluster profile and then further split into several images by two cluster members, resulting in a system of 7 multiple image candidates (shown in Fig. 3). The systems are included as in Di23 with a few modifications. We excluded K77.4 (as given in Di23) since it is indistinguishable from K33.4. We added our K77.4 candidate, which belongs to the same multiple image as K33.5. However, due to its uncertain position, we include it in the silver category. We included system candidate 110 from Di23 to system K33 as images K33.6 and K33.7. Of the two, we include K33.6 to our gold catalogue, following Be23. For image K33.7, which has not been included as a reliable candidate in previous studies, we provide a tentative spectroscopic confirmation based on the [OIII] emission line at around $2.1 \mu\text{m}$ in the grism spectra, shown in Fig. 3 (see also the NIRSpec spectrum of K33.1 in Fig. B.2). The emission can also be seen in other images of the system. This makes system K33 a very likely system with 7 multiple images. In this work, we add K33.7 to the silver category and do not use it to constrain the model.

4. Lens modelling

The strong lensing model was optimised using the parametric strong lens modelling software *Lenstool*³ (Kneib et al. 1996; Jullo et al. 2007; Jullo & Kneib 2009), which uses Markov Chain Monte-Carlo sampler *BayeSys* (Skilling 2004) to sample the posterior probability of the model parameters ξ . The posterior probability is computed as

$$P(\xi | \mathbf{r}^o) = P(\mathbf{r}^o | \xi) P(\xi), \quad (1)$$

where the prior probability $P(\xi)$ is the product of either uniform or Gaussian probabilities for each parameter. The likelihood $P(\mathbf{r}^o | \xi)$ given the positions of N multiple images \mathbf{r}^o , each with uncertainty σ_p is defined as

³ <https://projets.lam.fr/projects/lenstool/wiki/>

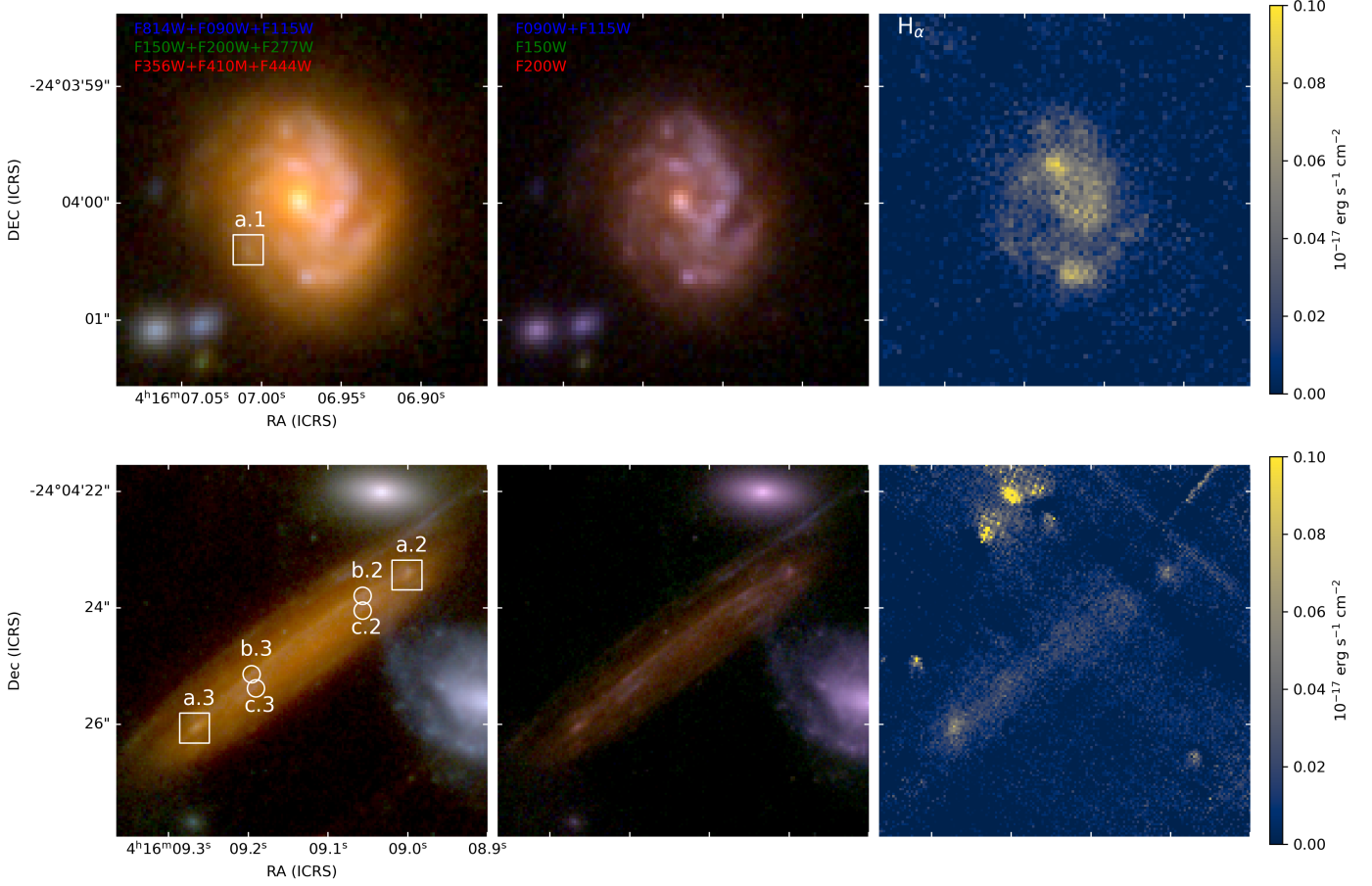


Fig. 2: Multiply imaged clumps a,b and c of system K8. The lower panels show the extended arc with two counter images of the spiral galaxy, shown in the upper panels. The two panels on the left show two RGB combinations of NIRC2 images. In the right panel, we show H_α emission line flux obtained from the F200W grism spectra (see Appendix A), which was used to identify image K8a.1.

Table 5: Images belonging to the old systems from Di23, added, updated or confirmed with our data. The asterisk (*) indicates relevant changes. Asterisk in the id means newly added counterimage, including the spectroscopically confirmed alternative to K26.3 image from Di23. We have updated the system redshift of systems K5 and K8 while also changing the exact position of K8a.1 (see Sect. 3.2). We spectroscopically confirmed K62b.3. The redshift uncertainty is estimated as $0.005(1+z)$ and $0.002(1+z)$ for z_{niriss} and z_{nirspec} , respectively (see Sects. 2.2 and 2.3).

id	ra	dec	z_{niriss}	z_{nirspec}	z_{sys}	class
K5.1	64.02388	-24.07761	1.84*		1.84*	(g)
K5.2	64.03056	-24.0827	1.84*			
K5.3	64.0325	-24.08377	1.84*			
K8a.1	64.029208*	-24.066782*	2.03*		2.04*	(g)
K8a.3	64.038610	-24.073900	2.04*	2.046*		
K26.3*	64.038267	-24.083734	2.92*		2.93	(g)
K62b.3	64.042139	-24.082314		5.14*	5.11	(g)
K81.3*	64.023671	-24.072630				(b)
K96.3*	64.037090	-24.062266				(b)

where χ^2 is calculated from the distance between the observed positions \mathbf{r}^o and model predicted positions \mathbf{r}^m :

$$P(\mathbf{r}^o|\boldsymbol{\xi}) = (2\pi\sigma_p^2)^{-\frac{N}{2}} \exp\left(-\frac{\chi^2(\mathbf{r}^o, \boldsymbol{\xi})}{2}\right), \quad (2) \quad \chi^2(\mathbf{r}^o, \boldsymbol{\xi}) = \sum_{j=1}^{n_{\text{sys}}} \sum_{i=1}^{n_{\text{im}}^j} \frac{\|\mathbf{r}_{i,j}^o - \mathbf{r}_{i,j}^m(\boldsymbol{\xi})\|^2}{\sigma_p^2}, \quad (3)$$

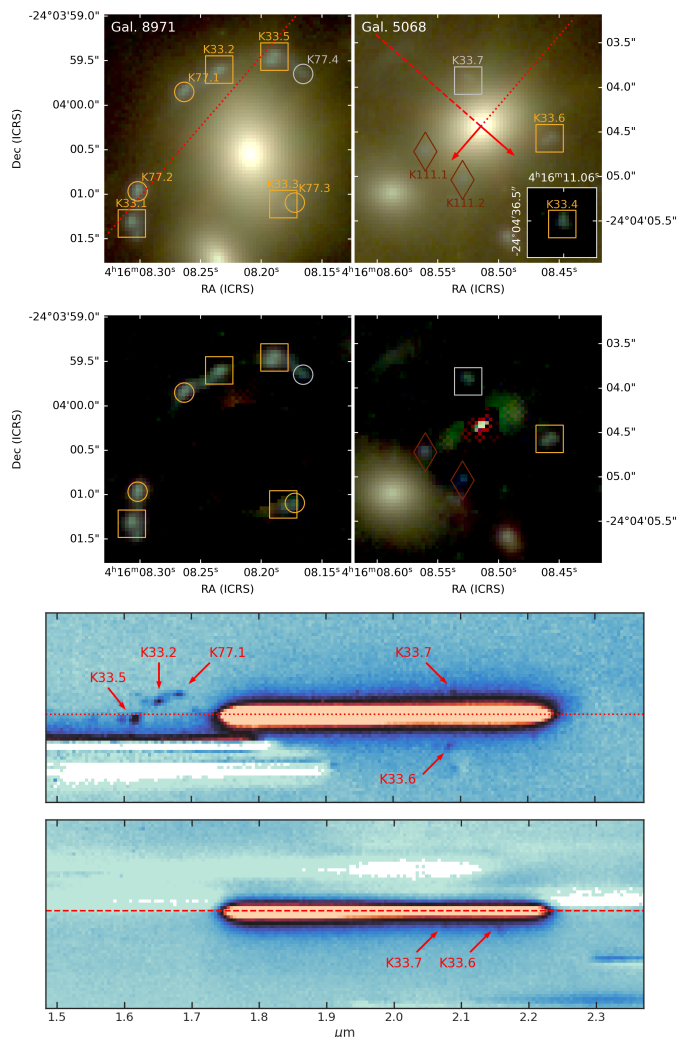


Fig. 3: Upper panel: RGB cutouts (with the same filter combinations as used in Fig. 1) of cluster members 8971 and 5068 with surrounding multiple image systems K33, K77 and K111. The inset cutout shows the counterimage K33.4. Gold, silver or bronze colours indicate the category (reliability) of multiple images. Dotted and dashed lines with arrows represent the orientation of 150C and 150R grism spectrum, respectively. They are also indicated on the bottom two panels. The dotted line indicating the 150C spectrum orientation extends to galaxy 8971, positioned $6''$ to the northeast of galaxy 5068. Second panel: RGB cutouts with removed cluster galaxies, enabling a better colour comparison. Third panel: F200W 150C grism spectrum of galaxy 5068 showing potential [OIII] emission lines observed at $2.1\mu\text{m}$ from K33.6 and K33.7, and emission from K33.2, K77.1 and K33.5 on the left. The wavelength calibration matches the spectrum of galaxy 5068. Fourth panel: F200W 150R grism spectrum of galaxy 5068, indicating the [OIII] emission of K33.6 and K33.7.

where the sum goes over n_{sys} multiple image systems, each containing n_{im}^j multiple images. For optimisation, Lenstool uses 10 interlinked chains to avoid local minima and varies the likelihood influence during the burn-in phase to control the convergence speed (see Jullo et al. 2007).

To evaluate the accuracy of the lens model we use the root-mean-square distance from the observed positions of multiple

images and positions predicted by the best model with parameters ξ_{best} :

$$\Delta_{\text{rms}} = \sqrt{\frac{1}{N} \sum_{i=1}^N \|r_i^o - r_i^m(\xi_{\text{best}})\|^2}. \quad (4)$$

In this work, we use the mass distribution parameterization from Be23, which was introduced as the best-performing lens model (LM-4HALOS) in Bergamini et al. (2021). It describes the total (baryonic and dark) matter distribution as a superposition of several elliptical halos with dual Pseudo Isothermal Elliptical (dPIE) density profile (Limousin et al. 2005; Elíasdóttir et al. 2007). Each dPIE halo is parametrised with 8 parameters: coordinates x and y of the centre, redshift z (set to 0.397 for all halos), ellipticity e , orientation θ , core radius r_{core} , cut radius r_{cut} and the Lenstool fiducial velocity dispersion σ_{lt} , which is related to central velocity dispersion σ_0 of the dPIE profile as $\sigma_{\text{lt}} = \sqrt{2/3}\sigma_0$. Positions x and y in this work are given in arcsec relative to the reference position $\alpha = 64.038142^\circ$, $\delta = -24.067472^\circ$, which coincides with the northern BCG. The total mass of each dPIE halo is computed as

$$M_{\text{tot}} = \frac{\pi\sigma_0^2}{G} \frac{r_{\text{cut}}^2}{r_{\text{cut}} + r_{\text{core}}}. \quad (5)$$

The global mass component in our lensing model features 4 large-scale cluster halos. Two are centred on the north-eastern and south-western BCGs with $30''$ and $15''$ wide uniform position priors, respectively (H1 and H2 in Fig. 4). Another halo is added to the southern region with a wider position prior as a second-order correction to the southern mass component (H4). A lower-mass halo H3 is added to the northeastern part of the cluster, coinciding with a smaller overdensity of cluster galaxies. In contrast to the other three cluster halos, H3 is added as a circular component without free ellipticity and orientation. All four cluster components have free σ_{lt} and r_{core} , while we fix their r_{cut} to a large value ($2000''$), as it cannot be constrained by the multiple images in the inner cluster regions.

All prior ranges of the free parameters are listed in the first part of Table 1 in Be23. Only one modification was required in the position prior of the H3 cluster halo, which had to be narrowed down to $-39'' < x < -25''$ and $2'' < y < 16''$. This modification proved necessary as the model with extended prior range ($-55'' < x < -25''$, $0'' < y < 30''$, see Be23) had problems with convergence after the addition of new spectroscopic systems - the model placed the 3rd cluster halo in a local minimum of χ^2 outside of the region covered with multiple images. After narrowing down the prior range, we found that the new solution, consistent with the best-fit position from Be23, yielded significantly better χ^2 and Δ_{rms} . We also note that the chosen prior range is nonetheless much larger than the 68% posterior confidence interval (see Table 6). This also further demonstrated the need for the additional mass component H3 in the overdensity of cluster galaxies to the northeast of the main cluster component (H1).

The model also includes four dPIE clumps describing the cluster gas distribution, derived from X-ray Chandra observations (Bonamigo et al. 2018, 2017). They are included as fixed clumps without free parameters, which is justified by a smaller set of assumptions when deriving the gas component mass distribution and smaller statistical errors compared to other components (Bonamigo et al. 2017). The parameters of the four clumps describing the cluster gas can be found in Table 1 of Be23.

Smaller subhalos, associated with cluster members, are modelled as circular dPIE profiles with vanishing core radius r_{core} . Cut radius $r_{\text{cut},i}$ and velocity dispersion $\sigma_{\text{lt},i}$ of each cluster member i scale with luminosity L_i of each galaxy according to the following relations (Jorgensen et al. 1996; Natarajan & Kneib 1997):

$$\sigma_{\text{lt},i} = \sigma_{\text{lt}}^{\text{ref}} \left(\frac{L_i}{L_{\text{ref}}} \right)^\alpha, \quad (6)$$

$$r_{\text{cut},i} = r_{\text{cut}}^{\text{ref}} \left(\frac{L_i}{L_{\text{ref}}} \right)^{\beta_{\text{cut}}}. \quad (7)$$

In this work, we use the cluster member catalogue with magnitudes from Bergamini et al. (2021), comprising 213 galaxies, 171 of which have spectroscopic confirmation. The positions of galaxies were first shifted to match the astrometry of CANUCS images (the correction was small, $\sim 0''.2$, and was also applied to the other mass components). The slopes of the scaling relations were derived in Bergamini et al. (2021), following the procedure described in Bergamini et al. (2019). They leverage measured velocity dispersions of cluster members with MUSE spectroscopy to obtain $\alpha = 0.3$, and derive $\beta_{\text{cut}} = 0.6$ by assuming that the subhalo mass $M_{\text{tot},i}$ scales with luminosity as $M_{\text{tot},i} \propto L_i^{0.2}$. As in Be23 and Bergamini et al. (2021), we assume a uniform prior between $1''$ and $50''$ for $r_{\text{cut}}^{\text{ref}}$, and a Gaussian prior for $\sigma_{\text{lt}}^{\text{ref}}$ centred at 248 km s^{-1} with standard deviation of 28 km s^{-1} . The Gaussian prior was determined with MUSE spectroscopy as described in Bergamini et al. (2019) and helps break the degeneracy between $\sigma_{\text{lt}}^{\text{ref}}$ and $r_{\text{cut}}^{\text{ref}}$, allowing for more accurate characterisation of the sizes of the cluster members. Luminosity L_i of the cluster members was estimated with *HST* F160W magnitudes from Bergamini et al. (2021), and for L_{ref} , the reference magnitude of 17.02 was chosen. As a test, we optimised a lens model of the upper half of the cluster (to reduce the dataset size and computational time). We used measured ellipticities instead of circular subhalos, as well as using NIRC*am* F090W magnitudes in place of F160W magnitudes. Neither case resulted in a χ^2 improvement compared to an identical run with the old cluster member catalogue; hence, we did not implement these changes in the final model. We leave the refinement of the cluster member catalogue with new *JWST* data for a future study, for instance, with new NIRISS spectroscopic catalogues of the full cluster field (Noirot et al., in prep.).

Two galaxy-scale halos were not modelled with scaling relations (equations 6 and 7). A foreground galaxy ($z=0.112$), which perturbs the lensing potential south of the H4 cluster halo, was modelled as a circular dPIE halo at the cluster redshift with free σ_{lt} and r_{cut} and vanishing r_{core} . Cluster member 8971 which produces the galaxy-galaxy lensing of systems K77 and K33 (left panel of Fig. 3, discussed in Sect. 3.2) was included as an elliptical dPIE halo with free ellipticity e , orientation θ , σ_{lt} and r_{cut} with vanishing r_{core} . See Table 1 in Be23 for the adopted prior values.

The parameter optimisation was done in two steps. For the first run of the model, we used the position uncertainty $\sigma_p = 0''.3$. We note that this is larger than the actual position uncertainty of the multiple images from the *HST* and *JWST* data. However, the actual accuracy ($\sim 40 \text{ mas}$) is beyond the current lens modelling capabilities, which do not consider contributions such as from the line-of-sight mass distribution or the scatter around the mass-to-light relation of the cluster galaxies (e.g. Jullo et al. 2010). The limitations of the lens model were further reflected in high

χ^2 values after the first run. After obtaining the minimum of χ^2 , we therefore rescaled the position uncertainties σ_p by a constant factor so that the minimal χ^2 was approximately equal to the number of degrees of freedom DoF:

$$\text{DoF} = 2N - 2n_{\text{sys}} - N_{\text{par}}. \quad (8)$$

N_{par} in equation 8 is the number of free parameters of the mass distribution (30 in this work) and $2n_{\text{sys}}$ is equal to the number of source positions of multiple image systems, which represent additional 222 free parameters. With $2N = 606$ measured coordinate positions of multiple images in our gold catalogue, we get $\text{DOF} = 354$. After rescaling σ_p so that $\chi^2/\text{DoF} \approx 1$ we reran the model. The position uncertainty used in the final optimization was $0''.49$. This rescaling is a standard practice in strong lensing studies (e.g. Be23, Grillo et al. 2016) and tries to account for systematic inaccuracies of the lens model. We emphasise that rescaling the uncertainty does not influence the best-fit model. It rather provides better-approximated uncertainties of model parameters.

After the 23 000 burn-in steps, during which the χ^2 value reached a stable value showing no significant average variation over large number of steps, we sampled the posterior with 30 000 samples. The best-fit model resulted in $\Delta_{\text{rms}} = 0''.53$. We do not use other fit quality criteria such as the BIC or AIC (e.g. see Bergamini et al. 2021) as the comparison of different model parameterizations is beyond the scope of this work. We also note the dependence of those criteria on the adopted σ_p , which does not reflect the uncertainty of the measurements in our case. In Table 6, we provide the median values and the 68% confidence intervals of the lensing model parameters. We note that the median parameter values may differ from the best model values, which we provide separately as a *Lenstool* parameter file on MAST. However, it enables a more straightforward comparison with the analogous table in Be23.

We also note that similar to the Bergamini et al. (2021) model, our model also predicts the multiple image K33.7, for which we provided a tentative spectroscopic confirmation in Sect. 3.2 and included it in the silver category. K33.7 is lensed by a cluster member with ID 5068, which is modelled with scaling relations (Equations 6 and 7).

5. Discussion

5.1. Comparison with Bergamini et al. (2023)

In Fig. 4 we show the positions of the main mass components as well the difference of convergence (κ) maps and the critical curves at redshift $z = 9$ between our and Be23 models. Comparing the new model parameter values with those from Be23, we can see that the 1st and the 3rd cluster halo parameters show minimal differences. The two halos are situated in the northern part of the cluster where the MUSE observations are the deepest, and our dataset includes fewer new multiple images than in the southern part (see Fig. 4). However, the addition of system K115, which is the most northeastern of the new multiple image systems and consists of an arc and a counterimage, required a slight modification of the 3rd cluster halo position prior range (see Sect. 4). The southern part of the cluster, consisting of the 2nd and the 4th cluster halo, shows more drastic differences from the Be23 model. The most striking difference is in the velocity dispersion σ_{lt} of the two halos. The velocity dispersion of the 2nd halo increased by $\sim 200 \text{ km s}^{-1}$ and the σ_{lt} of the 4th cluster halo decreased by a similar amount (see Table 6). This is reflected in the mass distribution, which shifted from the 2nd to the 4th cluster

Table 6: Optimised `Lenstool` parameters of the four cluster halos, scaling relations and two subhalos (galaxy 8971 and a foreground galaxy) which are modelled separately. Parameters with errorbars (indicating 68% confidence interval) were added as free parameters, while single values indicate fixed parameters. N_{gal} and $m_{\text{F160W}}^{\text{ref}}$ indicate the number of subhalos modelled with the scaling relations and the reference magnitude for which the reference parameters are given, respectively. The table is analogous to Table 1 in Be23. Positions x and y are given relative to the northern BCG.

	x ["]	y ["]	e	θ [°]	r_{core} ["]	σ_{lt} [km s ⁻¹]	r_{cut} ["]
1 st Cluster Halo	$-0.5^{+0.6}_{-0.5}$	$0.5^{+0.3}_{-0.4}$	$0.81^{+0.01}_{-0.01}$	$142.8^{+0.5}_{-0.6}$	$7.4^{+0.2}_{-0.2}$	590^{+9}_{-10}	2000.0
2 nd Cluster Halo	$22.1^{+0.3}_{-0.3}$	$-35.3^{+0.6}_{-0.5}$	$0.80^{+0.01}_{-0.01}$	$126.5^{+1.1}_{-0.7}$	$8.3^{+0.4}_{-0.6}$	670^{+21}_{-36}	2000.0
3 rd Cluster Halo	$-30.8^{+0.4}_{-0.4}$	$8.7^{+0.5}_{-0.4}$	0	0	$6.1^{+1.0}_{-1.0}$	328^{+23}_{-22}	2000.0
4 th Cluster Halo	$20.4^{+2.1}_{-2.3}$	$-51.2^{+1.6}_{-1.7}$	$0.83^{+0.03}_{-0.03}$	$131.5^{+1.3}_{-1.7}$	$11.5^{+0.9}_{-0.9}$	486^{+40}_{-32}	2000.0
Foreground. gal.	32.0	-65.6	0.0	0.0	0.0001	127^{+15}_{-31}	$34.4^{+29.3}_{-8.2}$
Gal-8971	13.3	2.6	$0.25^{+0.08}_{-0.05}$	$-54.8^{+19.4}_{-16.5}$	0.0001	111^{+3}_{-3}	$14.9^{+4.5}_{-4.5}$
Scaling relations	$N_{\text{gal}} = 212$	$m_{\text{F160W}}^{\text{ref}} = 17.02$	$\alpha = 0.30$	$\sigma_{\text{lt}}^{\text{ref}} = 199^{+2}_{-2}$	$\beta_{\text{cut}} = 0.60$	$r_{\text{cut}}^{\text{ref}} = 14.7^{+1.7}_{-1.3}$	$\gamma = 0.20$

halo (see Fig. 4). Another noticeable difference is in the scaling relation normalization of cluster halos - the reference velocity dispersion $\sigma_{\text{lt}}^{\text{ref}}$ decreased by ~ 30 km s⁻¹ compared to Be23. This is reflected in the systematic κ decrease in the vicinity of cluster members in Fig. 4.

We note that the Δ_{rms} of our dataset, which contains $> 20\%$ more multiply imaged systems, is larger from $\Delta_{\text{rms}} = 0''.43$ in Be23 by $\geq 20\%$. The small Δ_{rms} increase is not surprising, considering that the newly derived mass distribution accommodating the extended dataset differs from the one that minimised the χ^2 (and Δ_{rms}) of the old dataset using the same model parametrisation.

Despite the differences, we note the global mass distribution remains similar to Be23. In Fig. 4, we compare the position of the critical curve at high redshift. As the critical curves trace the regions of extreme magnification, their accurate description is vital for the studies of high redshift objects. In Fig. 4, we chose critical curves for sources at $z = 9$ to illustrate that the high redshift critical curves derived from the new model align well with those from Be23. The largest differences are found in the southernmost region which is constrained with fewer multiple images (see Fig. 1) - we note that there are no constraints south of the foreground galaxy.

5.2. The effectiveness of NIRISS for strong lensing studies

In Fig. 5, we show the redshift and F200W magnitude distribution of multiple images with spectroscopic system redshifts. Different markers and colours indicate whether system redshifts of multiple images could be measured with *JWST* (NIRISS or NIRSpec), MUSE or both. We also indicate the redshift ranges where the most significant emission lines fall in F115W, F150W or F200W grism spectrum. The redshift distribution of multiple images is shown in Fig. 6. Most new multiple images with NIRISS redshifts are found around redshifts 2 and 3 where at least two of the [OII], [OIII] and H α emission lines fall in the most sensitive range of the grism spectrum. In that range, NIRISS also successfully recovers most redshifts measured by MUSE.

Furthermore, we roughly estimate the expected redshift distribution of multiple image systems (red line in Fig. 6). This was done by first calculating the median distribution of photometric redshifts in the NIRCам flanking fields of all 5 CANUCS clusters. We considered all galaxies with reliable photometric red-

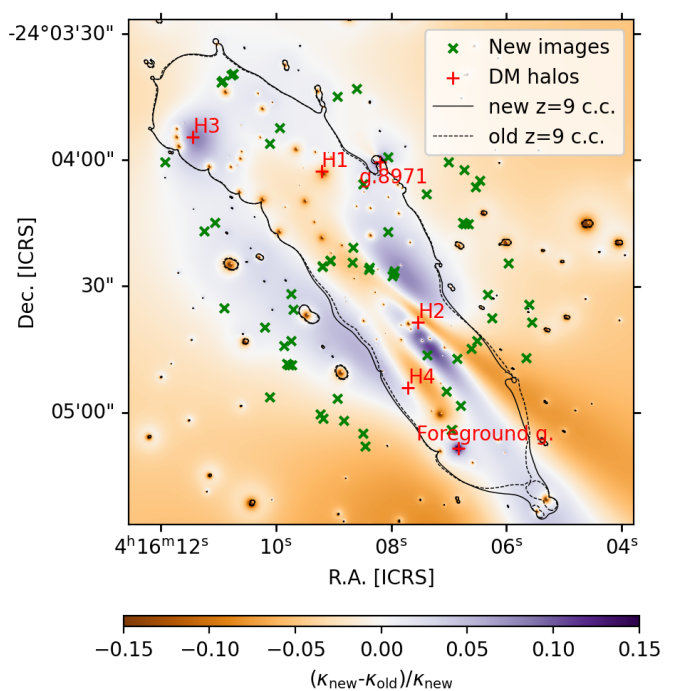


Fig. 4: Relative difference between the convergence (κ) from the updated strong lensing model with *JWST* data and the lens model from Be23 which uses the same parameterization. The positions of four main cluster halos (H1 to H4) and the two galaxies not included in the scaling relations (galaxy 8971 and the foreground galaxy) are marked with red pluses. Green crosses represent new multiple images and old multiple images with new spectroscopic redshift, not included in either Be23 or Di23 catalogue. Black solid and dashed lines represent the tangential (outermost) critical curve for sources at redshift 9, derived from the new and Be23 lensing models, respectively.

shifts regardless of their magnitudes. The redshift distribution of the sources peaks between redshift 1 and 2 due to the maximum angular diameter distance (and thus the largest volume covered by the same field-of-view). This unlensed distribution was then multiplied by the area of the multiply-imaged region in the source plane at each redshift. The area is equal to the area

bounded by the tangential caustics, which could be estimated with magnification and deflection maps produced by *Lenstool*. The area increases rapidly with redshift. The interplay between increasing lensed area, changing angular diameter distance and the decline in the number of detected sources with redshift results in a distribution that peaks at the redshift at which we expect to find the largest number of strongly lensed systems.

In Fig. 6, we show that in MACS0416, we expect to find most multiply lensed sources around redshift 2. At this redshift, [OII], [OIII] and H_α emission lines all fall in the range of our F115W, F150W and F200W grism spectra, making NIRISS spectroscopy ideal for finding multiple images up to faint magnitudes (even fainter than magnitude 27 in F200W filter, see Fig. 5). MUSE spectral range is, on the other hand, less ideal for this redshift range, as it cannot detect any of the above-mentioned emission lines above $z \sim 1.5$ and Lyman α emission below $z \sim 3$. Given sufficiently deep observation, such as in this cluster, MUSE is still effective at finding sources based on fainter emission lines (e.g. CIII] at 1907 Å, see the emission line catalogues from Richard et al. 2021). However it is evident that NIRISS grism spectroscopy, such as used in this work, complements even the deepest MUSE observations.

NIRISS grism spectroscopy also provides emission line maps of bright emission lines (e.g. H_α) with high spatial resolution, which can, in combination with photometry, help identify multiply-imaged clumps in extended multiple images and giant arcs. High magnifications in the giant arcs make them especially important for probing faint small-scale systems at high redshift. On the other hand, high magnification gradients near the critical curves make magnifications highly uncertain and any additional constraints invaluable. We demonstrated the use of emission line maps with system K8 (Fig. 2), where H_α flux complemented colour information, obtained with broadband NIRC*am* imaging. It helped us rule out some of the clumps with high H_α flux in the spiral galaxy as potential counter images of the brightest clump in the giant arc. We also point out that a significant fraction of systems, including some of the giant arcs (see Di23), are found in the redshift range where at least two of the [OII], [OIII] and H_α emission lines fall in our grism range (Fig. 5). Thus, this method could be extended from using individual emission line maps to using quantities such as emission line ratios, which are independent of magnification (provided they originate from the same source area) and could become a useful tool in future lensing studies.

In addition to NIRISS spectroscopy, this work also demonstrated the value of NIRSpec MSA prism spectroscopy for strong lens modelling. Its wide wavelength coverage enables redshift measurements from multiple emission lines in a wide redshift range (e.g. see the spectra in Fig. B.1). For instance, it allowed us to measure the redshift of system K100, $z_{\text{nirspec}} = 7.24 \pm 0.02$, which became the highest spectroscopic redshift of a multiple-image system in this cluster. However, unlike NIRISS and MUSE observations, NIRSpec MSA observations target pre-selected objects, which requires a reliable multiple-image candidate identification based on prior imaging data and photometric redshifts. Furthermore, if other follow-up targets are prioritised based on various science goals, not all multiple images can be observed due to the limited possible configurations of MSA masks. In this work, we obtained only one NIRSpec redshift per multiple image system (see Table 3). Although this is enough for determining the system redshift z_{sys} , it is, on its own, insufficient to confirm each multiply-imaged candidate. To assess the reliability of our gold multiple image systems, it was thus crucial to

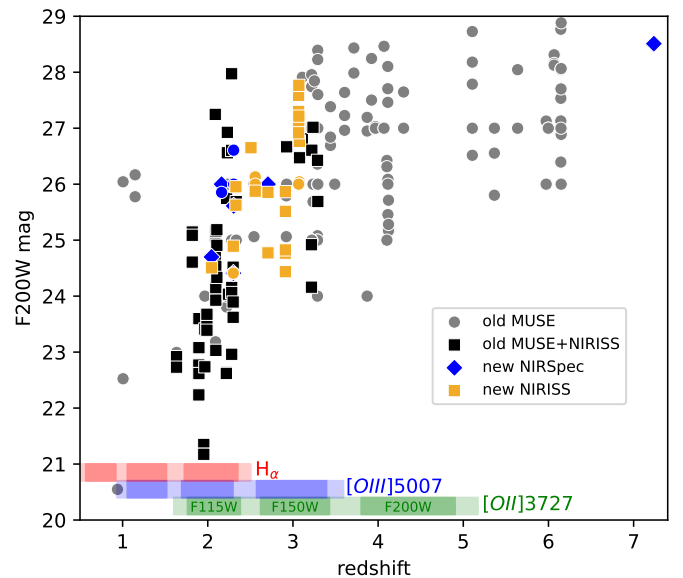


Fig. 5: Redshift and F200W magnitude of multiple images in our gold category with known spectroscopic redshifts. Images from Grey and black points represent known images with MUSE redshifts. For black squares, we also obtained NIRISS redshifts. Gold squares represent newly identified images for which we could obtain NIRISS redshift. Blue diamonds represent images without NIRISS but with NIRSpec redshift. Images for which the redshift could not be reliably measured but with measured system redshift from other images with NIRISS or NIRSpec are marked with gold and blue circles, respectively. Each multiple image is considered once (i.e. different clumps are not considered separately). The coloured bands at the bottom of the figure represent redshift ranges where some of the most prominent emission lines fall in the wavelength range, covered by each of the three NIRISS grism filters, used in this work. The darker shade of the grism range represents a more sensitive region (see Sect. 2.2).

use the NIRSpec data in combination with our imaging data and NIRISS spectroscopy.

6. Conclusion

In this work we present an updated strong lensing model of galaxy cluster MACS J0416.1-2403 (MACS0416) leveraging the new *JWST* imaging and spectroscopic data from the CANADIAN NIRISS Unbiased Cluster Survey (CANUCS). We expanded the existing catalogues of multiple images by searching for new multiple images in our NIRC*am* imaging data. To this end, we first predicted multiple images from sources in CANUCS photometric catalogues and then visually examined the region around each prediction in several *HST* and *JWST*/NIRC*am* RGB combinations. Our search independently discovered most of the already known candidates while also finding 15 previously unknown systems. The catalogue was further augmented by our spectroscopic redshift measurements. We examined the spectra obtained with NIRISS Wide-Field Slitless Spectroscopy of all our candidates and observed some of them with the NIRSpec multi-object prism spectroscopy. We measured spectroscopic redshift for 17 multiple image systems with previously unknown spectroscopic redshifts. We furthermore corrected the redshift of two known systems and confirmed two new counter

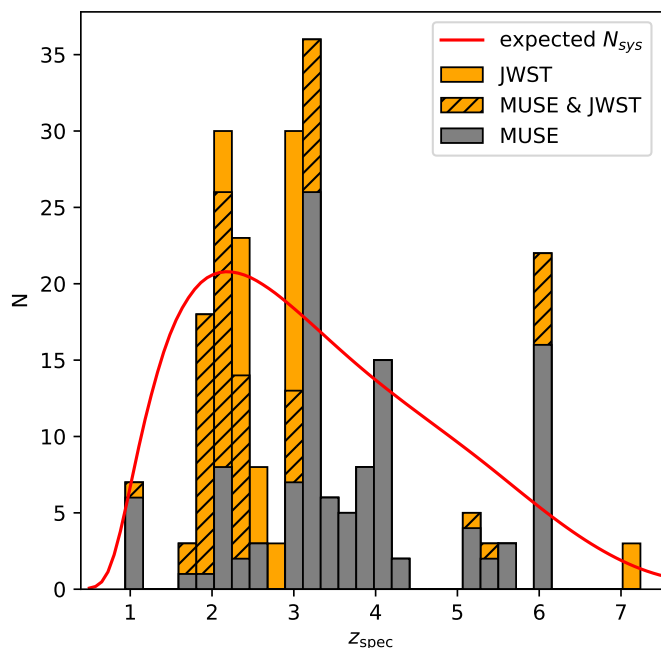


Fig. 6: Redshift distribution of multiple images, included in our gold catalogue, with known spectroscopic redshift. Images for which the spectroscopic redshift was obtained only by MUSE are shown in grey. Images for which we provided spectroscopic redshifts with *JWST* are shown in orange. Striped regions represent images with both *JWST* and MUSE redshift measurements. In the histogram, each multiple image is counted once (i.e. different multiply lensed clumps are not considered separately). The red solid line represents the expected redshift distribution of multiple image systems, considering the redshift distribution of sources in the field and multiply-imaged area in the source plane, which increases with redshift.

images of known systems. We also re-evaluated known sources with MUSE redshift (e.g. Be23, Richard et al. 2021, Bergamini et al. 2021, Caminha et al. 2017) and candidates found by previous studies, that used NIRC*am* imaging data (Di23). Our complete catalogue of all candidates comprises 415 multiple images belonging to 150 systems, 124 of which have known spectroscopic redshift. Out of those, we selected 303 reliable multiple images from 111 systems with spectroscopic redshift that we used for constraining the lens model (i.e. the gold catalogue). This makes our catalogue the largest catalogue of spectroscopic multiple images in a galaxy cluster field to date.

Our lens model was constrained using the parametric lens modelling code *Lenstool* with parameterization presented in Bergamini et al. (2021) and Be23. The new model shows accuracy $\Delta_{\text{rms}} = 0''.53$ and shows the largest difference from the Be23 pre-*JWST* lens model in the south-eastern region of the cluster, where we added most new constraints.

In this work, we also demonstrated the utility of NIRISS wide-field slitless spectroscopy in F115W, F150W and F200W filters for strong lensing studies. We show that such spectroscopy is the most effective at measuring redshifts between redshifts 2 and 3, where at least two of the three significant emission lines (H_{α} , [OIII] $\lambda\lambda 4959, 5007$ and [OII] $\lambda 3727$) can be detected. With a simple estimate, considering the redshift distribution of galaxies in the field and the multiply-lensed area as a function of redshift, we showed that this redshift range is particularly use-

ful for strong lensing studies, as it contains most multiple images. With system K8, we further demonstrated how spatially-resolved NIRISS spectroscopy and emission line maps can aid our understanding of extended multiple images and giant arcs. Since MACS0416 has been observed by some of the deepest *HST* imaging and MUSE spectroscopy programs, our study thus serves as a comparison between the results attainable with *JWST* and results currently attainable with the best ground or space-based facilities, using the largest known dataset in a single cluster.

We provide our catalogue of multiple images used to constrain the model and the full catalogue of multiple image candidates on CANUCS website (<https://niriss.github.io/>) together with the lens model presented in this work. Following the first CANUCS data release, the lens model will also be available on STScI Mikulski Archive for Space Telescopes (MAST) with DOI 10.17909/ph4n-6n76.

Acknowledgements. GR, MB, AH, VM and RT acknowledge support from the ERC Grant FIRSTLIGHT and from the Slovenian national research agency ARRS through grants N1-0238, P1-0188. MB acknowledges support from the program HST-GO-16667, provided through a grant from the STScI under NASA contract NAS5-26555. This research was enabled by grant 18JWST-GTO1 from the Canadian Space Agency and funding from the Natural Sciences and Engineering Research Council of Canada. This research used the Canadian Advanced Network For Astronomy Research (CANFAR) operated in partnership by the Canadian Astronomy Data Centre and The Digital Research Alliance of Canada with support from the National Research Council of Canada the Canadian Space Agency, CANARIE and the Canadian Foundation for Innovation.

References

- Adamo, A., Bradley, L. D., Vanzella, E., et al. 2024, arXiv e-prints, arXiv:2401.03224
- Asada, Y., Sawicki, M., Abraham, R., et al. 2024, MNRAS, 527, 11372
- Asada, Y., Sawicki, M., Desprez, G., et al. 2023, MNRAS, 523, L40
- Bacon, R., Accardo, M., Adjali, L., et al. 2012, The Messenger, 147, 4
- Balestra, I., Mercurio, A., Sartoris, B., et al. 2016, ApJS, 224, 33
- Bergamini, P., Grillo, C., Rosati, P., et al. 2023, A&A, 674, A79
- Bergamini, P., Rosati, P., Mercurio, A., et al. 2019, A&A, 631, A130
- Bergamini, P., Rosati, P., Vanzella, E., et al. 2021, A&A, 645, A140
- Bonamigo, M., Grillo, C., Ettori, S., et al. 2017, ApJ, 842, 132
- Bonamigo, M., Grillo, C., Ettori, S., et al. 2018, ApJ, 864, 98
- Bradač, M., Strait, V., Mowla, L., et al. 2024, ApJ, 961, L21
- Bradley, L., Sipőcz, B., Robitaille, T., et al. 2023, astropy/photutils: 1.7.0, <https://doi.org/10.5281/zenodo.7804137>
- Brammer, G. 2022, gbrammer/msaexp: Full working version with 2d drizzling and extraction, <https://doi.org/10.5281/zenodo.7299501>
- Brammer, G. 2023, grizli, <https://doi.org/10.5281/zenodo.8210732>
- Brammer, G. B., van Dokkum, P. G., & Coppi, P. 2008, ApJ, 686, 1503
- Bunker, A. J., Cameron, A. J., Curtis-Lake, E., et al. 2023, arXiv e-prints, arXiv:2306.02467
- Caminha, G. B., Grillo, C., Rosati, P., et al. 2017, A&A, 600, A90
- Caminha, G. B., Suyu, S. H., Grillo, C., & Rosati, P. 2022a, A&A, 657, A83
- Caminha, G. B., Suyu, S. H., Mercurio, A., et al. 2022b, A&A, 666, L9
- Chen, W., Kelly, P. L., Diego, J. M., et al. 2019, ApJ, 881, 8
- Desprez, G., Martis, N. S., Asada, Y., et al. 2024, MNRAS, 530, 2935
- Diego, J. M., Adams, N. J., Willner, S., et al. 2023a, arXiv e-prints, arXiv:2312.11603
- Diego, J. M., Broadhurst, T., Molnar, S. M., Lam, D., & Lim, J. 2015, MNRAS, 447, 3130
- Diego, J. M., Kei Li, S., Meena, A. K., et al. 2023b, arXiv e-prints, arXiv:2304.09222
- Diego, J. M., Sun, B., Yan, H., et al. 2023c, A&A, 679, A31
- Doyon, R., Hutchings, J. B., Beaulieu, M., et al. 2012, in Society of Photo-Optical Instrumentation Engineers (SPIE) Conference Series, Vol. 8442, Space Telescopes and Instrumentation 2012: Optical, Infrared, and Millimeter Wave, ed. M. C. Clampin, G. G. Fazio, H. A. MacEwen, & J. Oschmann, Jacobus M., 84422R
- Drlica-Wagner, A., Sevilla-Noarbe, I., Rykoff, E. S., et al. 2018, ApJS, 235, 33
- Ebeling, H., Edge, A. C., Mantz, A., et al. 2010, MNRAS, 407, 83
- Elíasdóttir, Á., Limousin, M., Richard, J., et al. 2007, arXiv e-prints, arXiv:0710.5636
- Estrada-Carpenter, V., Sawicki, M., Brammer, G., et al. 2024, MNRAS

- Fudamoto, Y., Sun, F., Diego, J. M., et al. 2024, arXiv e-prints, arXiv:2404.08045
- Fujimoto, S., Ouchi, M., Kohno, K., et al. 2024, arXiv e-prints, arXiv:2402.18543
- Furtak, L. J., Meena, A. K., Zackrisson, E., et al. 2024, MNRAS, 527, L7
- Furtak, L. J., Zitrin, A., Weaver, J. R., et al. 2023, MNRAS, 523, 4568
- Gaia Collaboration, Brown, A. G. A., Vallenari, A., et al. 2016, A&A, 595, A2
- Gaia Collaboration, Vallenari, A., Brown, A. G. A., et al. 2023, A&A, 674, A1
- Gledhill, R., Strait, V., Desprez, G., et al. 2024, arXiv e-prints, arXiv:2403.07062
- Grillo, C., Karman, W., Suyu, S. H., et al. 2016, ApJ, 822, 78
- Grillo, C., Suyu, S. H., Rosati, P., et al. 2015, ApJ, 800, 38
- Hashimoto, T., Laporte, N., Mawatari, K., et al. 2018, Nature, 557, 392
- Hoag, A., Huang, K. H., Treu, T., et al. 2016, ApJ, 831, 182
- Jauzac, M., Clément, B., Limousin, M., et al. 2014, MNRAS, 443, 1549
- Jauzac, M., Jullo, E., Eckert, D., et al. 2015, MNRAS, 446, 4132
- Johnson, T. L. & Sharon, K. 2016, ApJ, 832, 82
- Johnson, T. L., Sharon, K., Bayliss, M. B., et al. 2014, ApJ, 797, 48
- Jorgensen, I., Franx, M., & Kjaergaard, P. 1996, MNRAS, 280, 167
- Jullo, E. & Kneib, J. P. 2009, MNRAS, 395, 1319
- Jullo, E., Kneib, J. P., Limousin, M., et al. 2007, New Journal of Physics, 9, 447
- Jullo, E., Natarajan, P., Kneib, J. P., et al. 2010, Science, 329, 924
- Kaurov, A. A., Dai, L., Venumadhav, T., Miralda-Escudé, J., & Frye, B. 2019, ApJ, 880, 58
- Kawamata, R., Oguri, M., Ishigaki, M., Shimasaku, K., & Ouchi, M. 2016, ApJ, 819, 114
- Kelly, P. L., Chen, W., Alfred, A., et al. 2022, arXiv e-prints, arXiv:2211.02670
- Kneib, J. P., Ellis, R. S., Smail, I., Couch, W. J., & Sharples, R. M. 1996, ApJ, 471, 643
- Kron, R. G. 1980, ApJS, 43, 305
- Larson, R. L., Hutchison, T. A., Bagley, M., et al. 2023, ApJ, 958, 141
- Limousin, M., Kneib, J.-P., & Natarajan, P. 2005, MNRAS, 356, 309
- Lotz, J., Mountain, M., Grogin, N. A., et al. 2014, in American Astronomical Society Meeting Abstracts, Vol. 223, American Astronomical Society Meeting Abstracts #223, 254.01
- Lotz, J. M., Koekemoer, A., Coe, D., et al. 2017, ApJ, 837, 97
- Magaña, J., Acebrón, A., Motta, V., et al. 2018, ApJ, 865, 122
- Mahler, G., Jauzac, M., Richard, J., et al. 2023, ApJ, 945, 49
- Mann, A. W. & Ebeling, H. 2012, MNRAS, 420, 2120
- Martis, N. S., Sarrouh, G. T. E., Willott, C. J., et al. 2024, arXiv e-prints, arXiv:2401.01945
- Meena, A. K., Zitrin, A., Jiménez-Teja, Y., et al. 2023, ApJ, 944, L6
- Mowla, L., Iyer, K., Asada, Y., et al. 2024, arXiv e-prints, arXiv:2402.08696
- Natarajan, P. & Kneib, J.-P. 1997, MNRAS, 287, 833
- Natarajan, P., Williams, L. L. R., Bradač, M., et al. 2024, Space Sci. Rev., 220, 19
- Noiro, G., Desprez, G., Asada, Y., et al. 2023, MNRAS, 525, 1867
- Oke, J. B. & Gunn, J. E. 1983, ApJ, 266, 713
- Postman, M., Coe, D., Benítez, N., et al. 2012, ApJS, 199, 25
- Refsdal, S. 1964, MNRAS, 128, 307
- Richard, J., Claeysens, A., Lagattuta, D., et al. 2021, A&A, 646, A83
- Schmidt, K. B., Treu, T., Brammer, G. B., et al. 2014, ApJ, 782, L36
- Skilling, J. 2004, BayeSys and MassInf
- Steinhardt, C. L., Jauzac, M., Acebron, A., et al. 2020, ApJS, 247, 64
- Strait, V., Brammer, G., Muzzin, A., et al. 2023, ApJ, 949, L23
- Tanaka, M., Coupon, J., Hsieh, B.-C., et al. 2018, PASJ, 70, S9
- Treu, T., Schmidt, K. B., Brammer, G. B., et al. 2015, ApJ, 812, 114
- Vanzella, E., Caminha, G. B., Rosati, P., et al. 2021, A&A, 646, A57
- Vanzella, E., Castellano, M., Meneghetti, M., et al. 2017, ApJ, 842, 47
- Vanzella, E., Loiacono, F., Bergamini, P., et al. 2023, A&A, 678, A173
- Welch, B., Coe, D., Diego, J. M., et al. 2022, Nature, 603, 815
- Welch, B., Coe, D., Zitrin, A., et al. 2023, ApJ, 943, 2
- Willott, C. J., Doyon, R., Albert, L., et al. 2022, PASP, 134, 025002
- Windhorst, R. A., Cohen, S. H., Jansen, R. A., et al. 2023, AJ, 165, 13
- Withers, S., Muzzin, A., Ravindranath, S., et al. 2023, ApJ, 958, L14
- Yan, H., Ma, Z., Sun, B., et al. 2023, ApJS, 269, 43
- Zitrin, A., Meneghetti, M., Umetsu, K., et al. 2013, ApJ, 762, L30

Appendix A: Grism spectra

In Figs. A.1, A.2, A.2, A.2 and A.3 we provide NIRISS grism spectra used to obtain spectroscopic redshifts of multiple images in this work. All fits, apart from K87.2, used only the grism spectrum. For K87.2, only the combined fit of the grism spectrum and photometry returned the correct redshift in agreement with K87.1 and K87.3. We note that its spectrum contains clear [OIII] and [OII] emission in agreement with other images of the system. Images K95.1, K95.3, K90.1, K90.3 and C2.3 were re-fitted with a narrower redshift prior (± 1 or ± 0.5) where the redshift range was estimated based on other images of the system with more reliable fits (grism or NIRSpec prism) and corroborated by other arguments (several visually discernible emission lines, photometric redshifts etc.). We note that the grism redshifts of those images agree with other images of the system within the spectroscopic redshift uncertainty, which is much narrower than the chosen prior range. We also note that GR150C grism orientation in K82.1 is aligned with the direction of the arc, resulting in a collapsed 1D spectrum without visible emission lines. However, GR150R orientation shows several emission lines and the combined fit of a narrow spectral range returns a reliable redshift of 2.03 ± 0.02 .

Appendix B: NIRSpec spectra

In Figs. B.1 and B.2 we show the NIRSpec prism spectra used for obtaining our updated multiple image catalogue. The reduction and redshift extraction is outlined in Sect. 2.3. In the following, we describe two cases where `msaexp` fitting with wide redshift prior did not produce satisfying results. In the spectrum of K82.2 we find a noticeable emission line consistent with [OIII] emission in K82.1 grism spectrum (Fig. A.2, different part of the same arc), thus, we fit the image with a narrow redshift prior between 1.8 and 2.4, obtaining a redshift of 2.053. The spectrum of K89.3 shows an H_α emission line, consistent with redshift obtained from [OII] and [OIII] emission lines in the grism spectrum of the same image, shown in Fig. A.2 (the spectral range containing [OII] and [OIII] lines is missing in the NIRSpec spectrum). As the full spectral fit could not produce reliable redshift, we fitted the H_α emission line with a Gaussian profile and obtained the best redshift of 3.082 ± 0.008 .

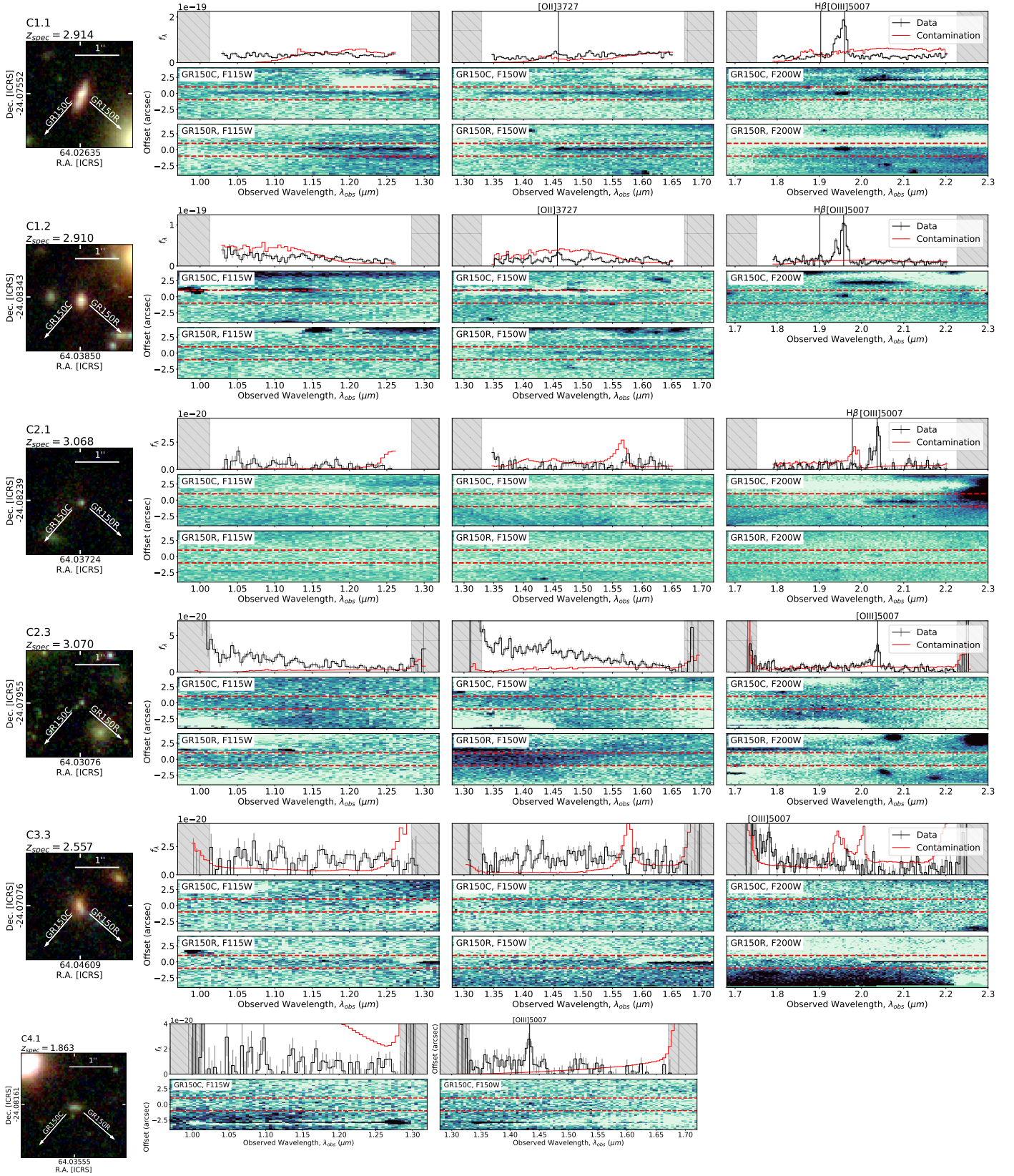


Fig. A.1: NIRISS F115W and F150W and F200W grism spectra of the newly discovered (CANUCS) multiple images. The RGB cutouts are composed of *JWST*/NIRCam and *HST*/WFC3 images (F277W, F356W, F410M, F444W in red, F115W, F150W, F200W in green and F814W, F606W, F435W and F090W in blue) with indicated angular scale and the GR150R and GR150C grism dispersion directions. The upper row represents 1D spectra in different filters, showing only the spectral range used for redshift fitting (see Sect. 2.2). The plots include contamination and some of the prominent emission lines, and the grey-shaded region represents the spectral range where the filter transmission falls below one-half of the maximal value. The second and the third row include 2D spectra in each band, and for each orientation used to obtain redshift - highly contaminated spectra are not displayed.

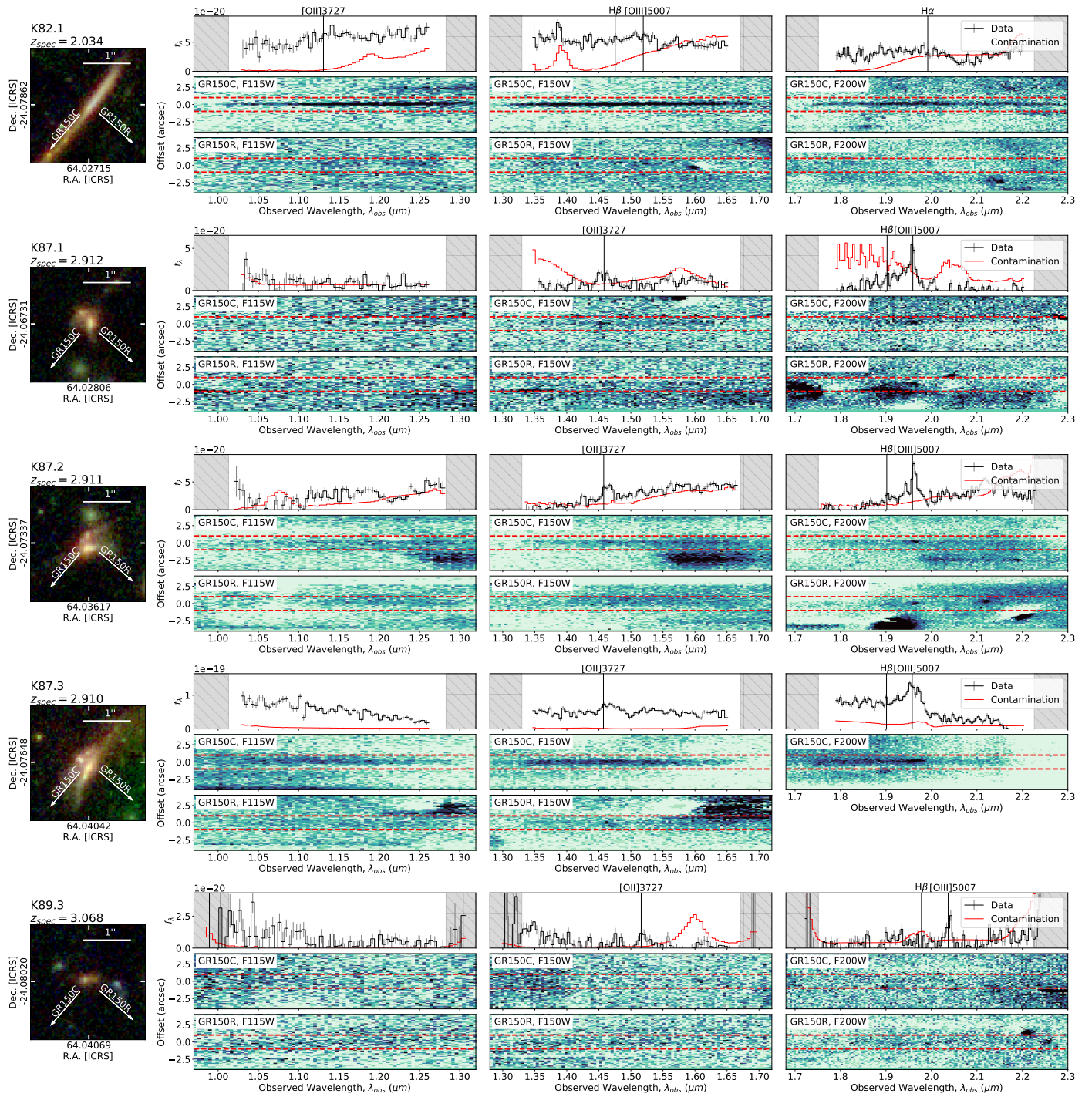


Fig. A.2: NIRISS spectra of known multiple image candidates with previously unknown system redshift. The figure is analogous to Fig. A.1.

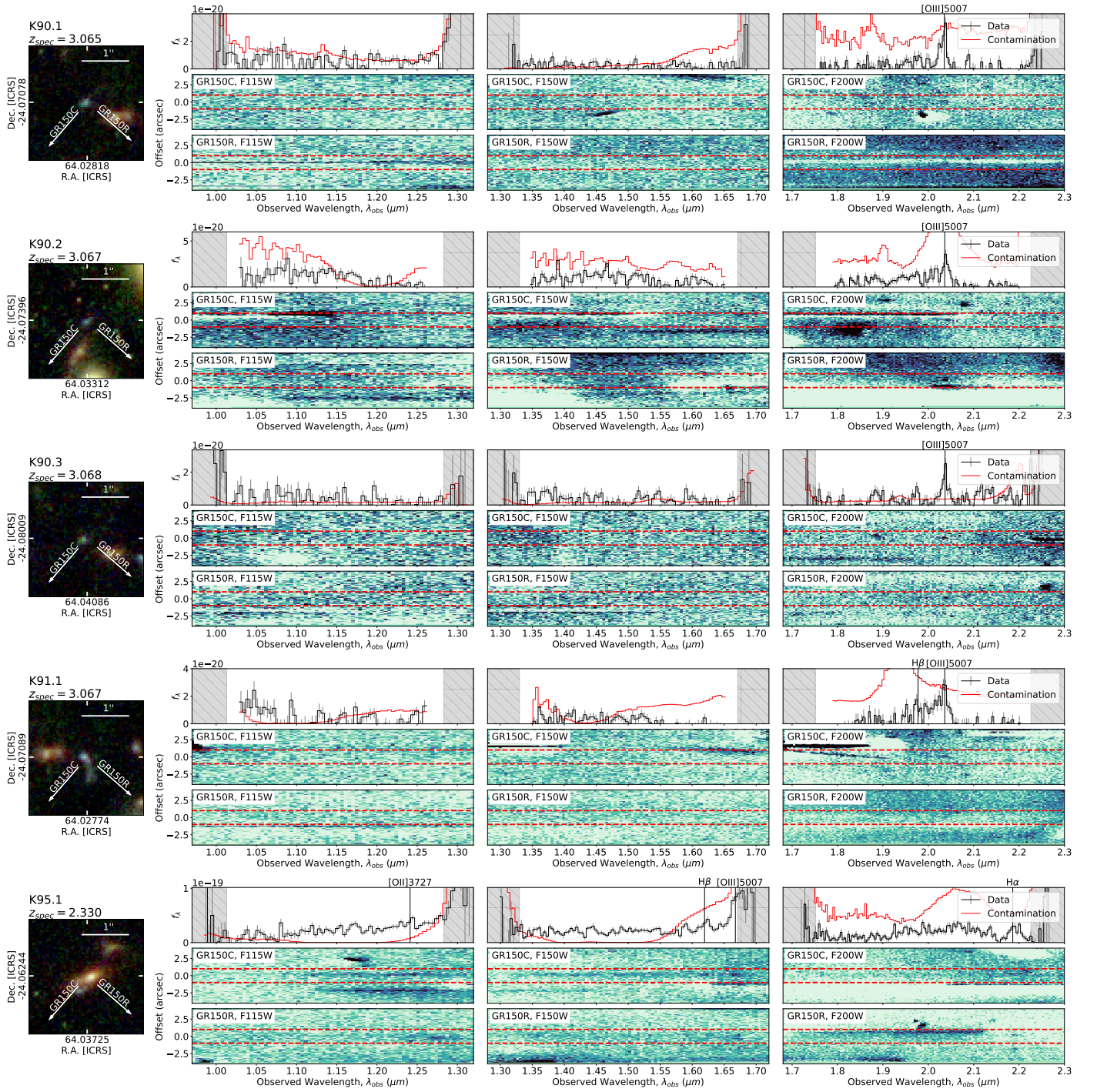


Fig. A.2: continued

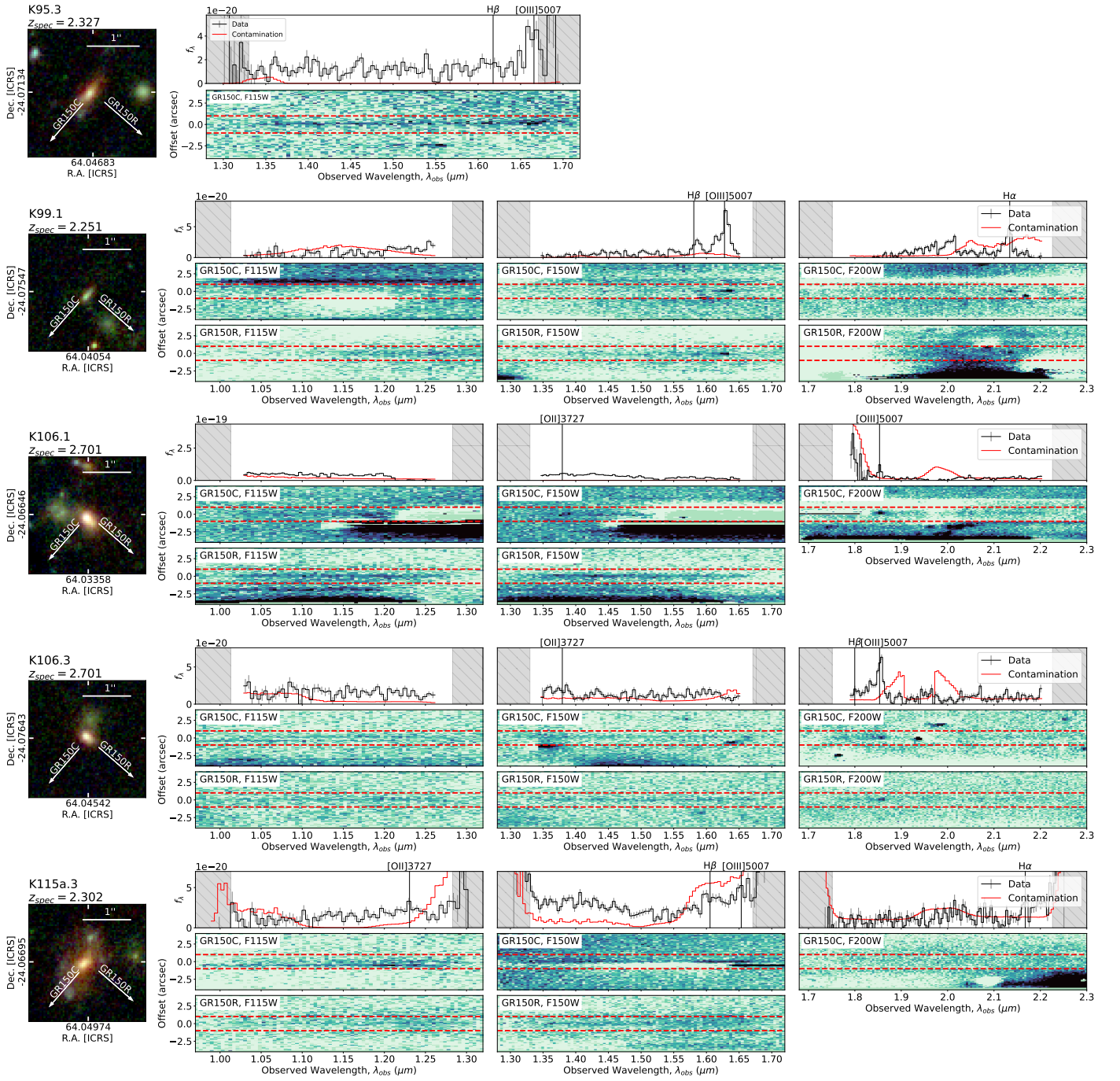


Fig. A.2: continued

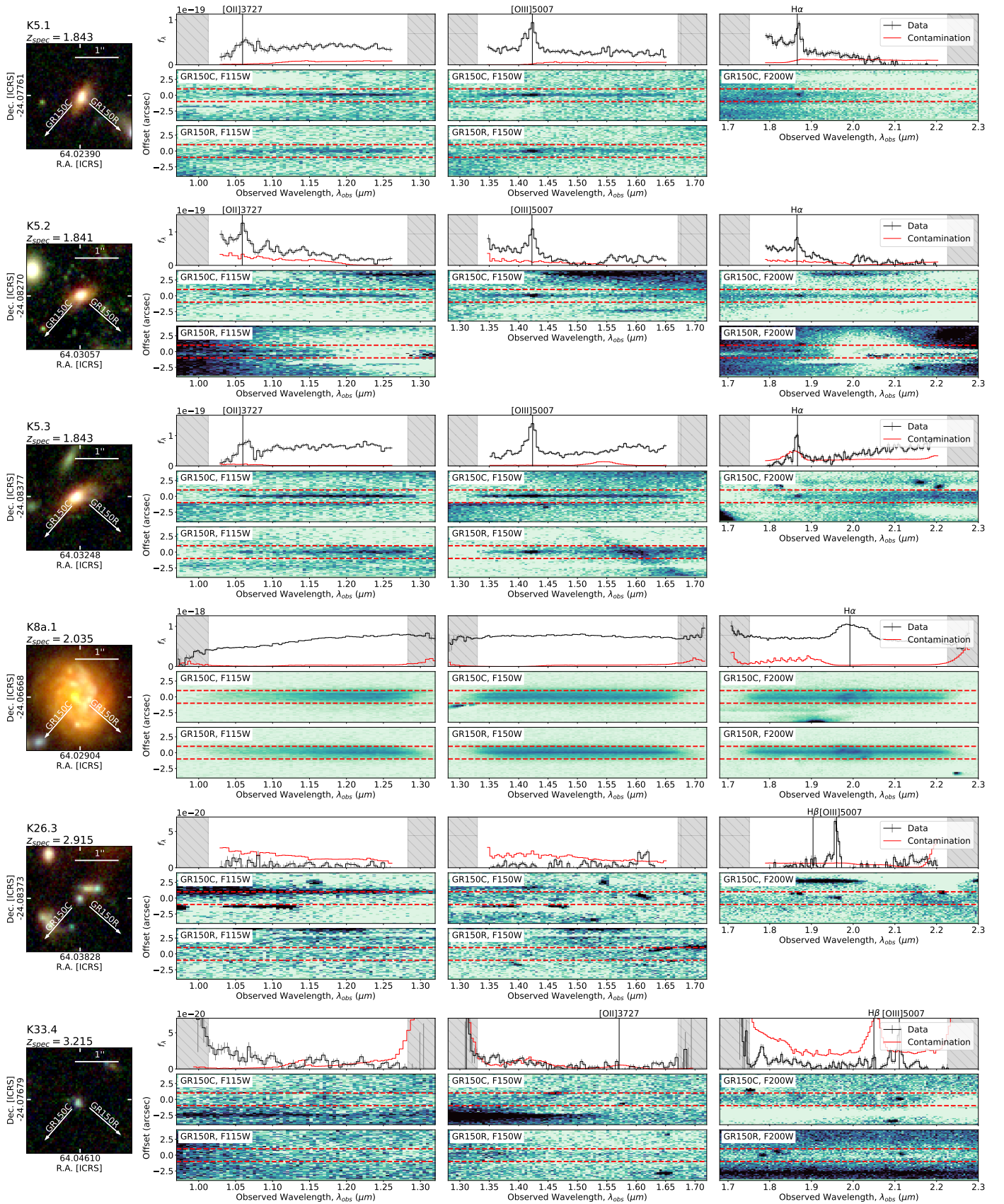


Fig. A.3: NIRISS spectra, not included in previous figures but also used in this work, either for updating the system redshift (K5 and K8a.1), confirming a new multiple image candidate (K26.3) or showing the spectral line found in other counter images (K33.4). The figure is analogous to Figs. A.1 and A.2.

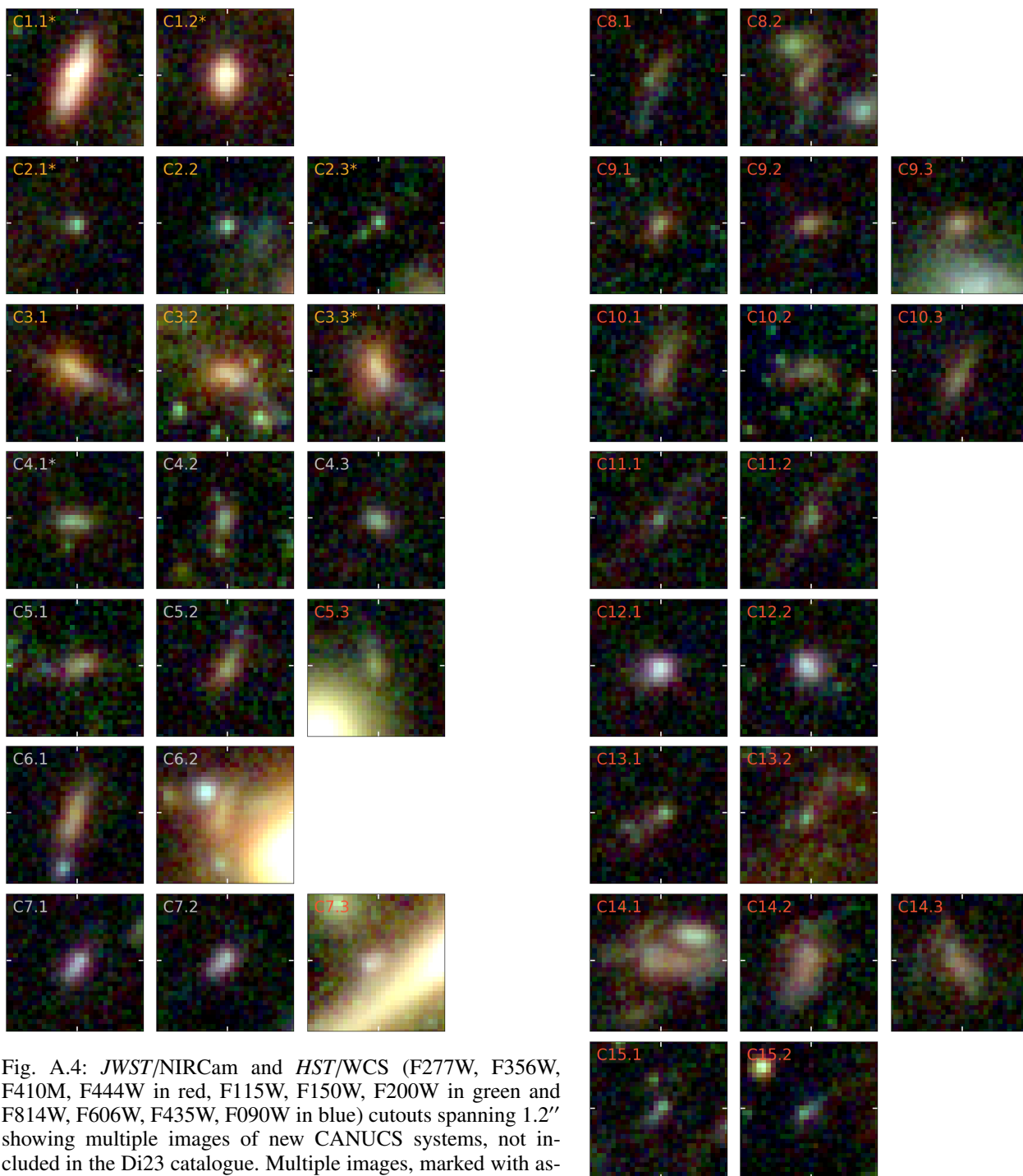


Fig. A.4: *JWST*/NIRCam and *HST*/WCS (F277W, F356W, F410M, F444W in red, F115W, F150W, F200W in green and F814W, F606W, F435W, F090W in blue) cutouts spanning $1.2''$ showing multiple images of new CANUCS systems, not included in the Di23 catalogue. Multiple images, marked with asterisk (*) are spectroscopically confirmed and are also shown in Fig. A.1 with their grism spectra. The colour of the labels indicates the category (gold, silver, or bronze, depending on their reliability).

Fig. A.4: continued

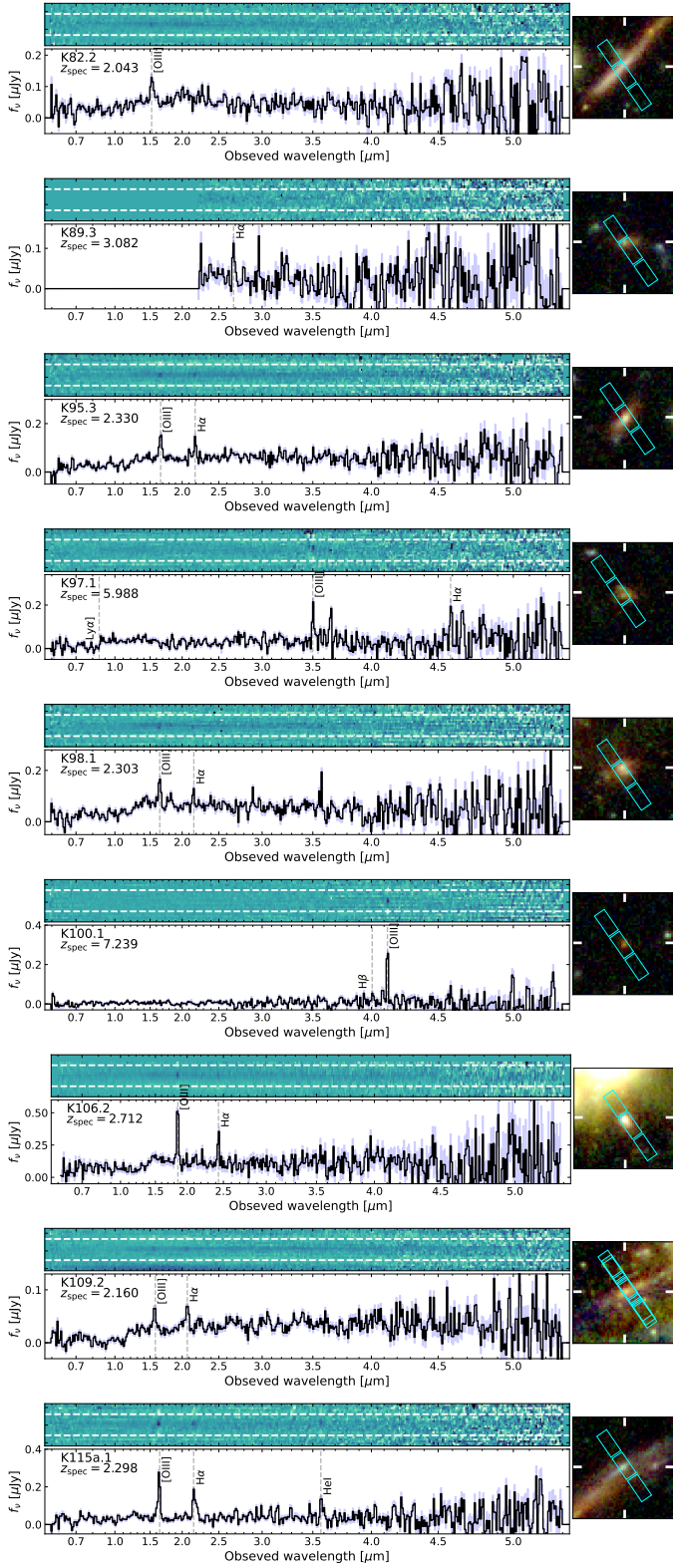


Fig. B.1: 2D and 1D NIRSpec prism spectra of multiple images with previously unknown system redshift. Vertical dashed lines indicate some of the prominent emission lines. The cutouts show the RGB composition of *JWST*/NIRCam and *HST*/WFC3 images (F277W, F356W, F410M, F444W in red, F115W, F150W, F200W in green and F814W, F606W, F435W and F090W in blue) with the size of $2''$. Cyan rectangles indicate the MSA slit positions.

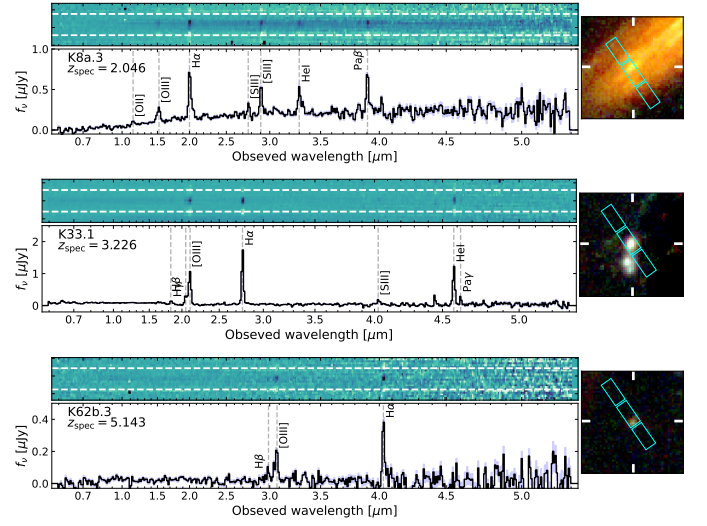


Fig. B.2: 2D and 1D NIRSpec prism spectra, not included in Fig. B.1 but also used in this work, either for updating the system redshift (K8a.3), confirming a new multiple image candidate (K62b.3) or for showing the emission line, detected in the grism spectra of the counter images (K33.1).